MASTER'S THESIS
JULY 2015

Universiteit Utrecht

Reconstructing reversal frequencies: constraints on core-mantle boundary heat flow evolution

Maurits C. Metman[1,2,*]

[1]Paleomagnetic Laboratory Fort Hoofddijk, Department of Earth Sciences, Budapestlaan 17, 3584 CD Utrecht, The Netherlands
[2]Theoretical Geophysics research group, Department of Earth Sciences, Heidelberglaan 2, 3584 CS Utrecht, The Netherlands

Abstract

The core-mantle boundary heat flow controls the geodynamo and in particular the occurrence of geomagnetic reversals. Unfortunately, the present-day and past core-mantle boundary heat flow are poorly constrained. In this work, a series of numerical dynamo models put constraints on the core-mantle boundary heat flow evolution for the past 270 Myr by comparing the reversal frequencies from those models with observations. A benchmark is performed to ensure the correct installation of the code used to run the simulations. The present-day reversal frequency of $\sim$4 Myr^{-1} is reproduced to find a dynamo model representative of the current geodynamo state. By varying the Rayleigh number Ra_Q, an initial dynamo model with $Ra_Q = 1.26 \cdot 10^{-4}$ yielded a frequency of 3.85 Myr^{-1}. Geodynamo evolution is modelled by applying estimates of secular changes in geodynamo control parameters to the initial model. Several scenarios for the evolution of the core-mantle heat flow were imposed, which are validated by comparing computed reversal frequencies with the reversal record. Heat flow evolution scenarios from mantle convection reconstructions and a linear decrease of heat flow with time were employed. It was found that secular changes in the heat flow have been in the order of 1% and not more than 7.5% compared to the time-average heat flow. Moreover, the results indicate that the core-mantle boundary heat flow has decreased linearly with time, from roughly 18 to 15 TW over the past 270 Myr.

Keywords: geodynamo, CMB heat flow, reversals, reconstruction, numerical modelling

1. Introduction

The principle that the magnetic field encompassing a celestial body may be generated through motions within that body, is almost a century old (Larmor, 1919). This idea was initially applied to the Sun and its magnetic field, although it proved to be applicable to the Earth. At the present day, it is generally accepted that Earth's magnetic (*geomagnetic*) field is the result of a liquid, convecting and electrically conducting iron alloy in the Earth's outer core - a mechanism that is generally referred to as the *geodynamo* (see e.g. Olson, 2007).

The geodynamo is strongly controlled by the heat flux through the core-mantle boundary (CMB). In particular, the CMB heat flux can trigger geomagnetic *reversals*, i.e. spontaneous reversals of the polarity of the magnetic field. The occurrence of reversals is often expressed in terms of the amount of reversals occurring per unit time, or *reversal frequency*. The reversal frequency is low when the heterogeneity of the CMB heat flow is small, the largest part of the CMB heat flow is expelled at the poles and/or equator and when a symmetry of the CMB heat flow about the equator is strongly present (Glatzmaier et al., 1999). More dominant in reversal control than the distribution of heat flow across the CMB is the CMB heat flow magnitude or total thermal power transferred from the core to the mantle Q_{cmb}, where the total heat flow and the occurence of reversals are positively correlated (Olson et al., 2010; Driscoll and Olson, 2011). Also, the strength of the dipolar component of the geomagnetic field, often expressed in terms of *dipole moment*, has been shown to decrease with Q_{cmb}, such that reversal frequency and the dipole moment appear to be anti-correlated (Driscoll and Olson, 2011). In contrast to Glatzmaier et al. (1999), Olson et al. (2010) demonstrated that an equatorial heat flux has a destabilising effect. In any case, a link between the magnitude and heterogeneity of the CMB heat flux magnitude and the reversibility of the geomagnetic field is evident.

The ongoing debate concerning the thermal and electrical conductivity of the outer core additionally illustrates the importance of the CMB heat flow for the geodynamo. These conductivities are shown to be larger than previous estimates by a factor two to three (Pozzo et al., 2011). This implies that the conductive heat transported across the upper outer core is larger than the current CMB heat flux. Then, the core temperature gradient near the CMB should be smaller and subadiabatic, stratifying the outermost core (Buffett, 2012). Thus, an accurate estimate of Q_{cmb} can help determine whether the outermost core is convecting at all. This elaboration illustrates how not only the magnetic dynamics (e.g. in terms of reversals), but also the thermal dynamics of the geodynamo are sensitive to the CMB heat flow.

Unfortunately, the present-day CMB heat flow is poorly constrained. Traditionally, Q_{cmb} has been estimated as low as 3 TW. However, more recent estimates range from 5 to 15 TW, corresponding to a CMB surface average heat flow $\overline{q}$ between 33 and 98 mW m^{-2} (Lay et al., 2008). The heat flow heterogeneity across the CMB δq can be expressed as:

$$\delta q = \frac{q_{\mathrm{max}} - q_{\mathrm{min}}}{2\overline{q}} \tag{1}$$

where q_{max} and q_{min} are the local maxima and minima in CMB heat flow (Olson and Christensen, 2002). As follows from this definition, δq is also poorly constrained. Numerical reconstructions of mantle convection show that when thermochemical piles are superimposed on the CMB $\delta q \sim 0.4$; beneath slab remnants this heterogeneity can be as high as $\delta q \sim 2$ (Biggin et al., 2012).

As the present-day CMB heat flow distribution is not well constrained, heat flow distributions during earlier times in Earth's evolution have even larger uncertainties. Despite this, estimates of secular changes in the CMB heat flow have been made. For example, Labrosse et al. (2007) proposed a heat flow evolution model assuming the existence of a long-lived magmatic ocean at the base of the mantle. They prefer a model of linear increase with age in CMB heat flow

*Corresponding author, email address: M.C.Metman@students.uu.nl.
This work was performed under the supervision of dr. L. V. de Groot[1] and dr. C. Thieulot[2]

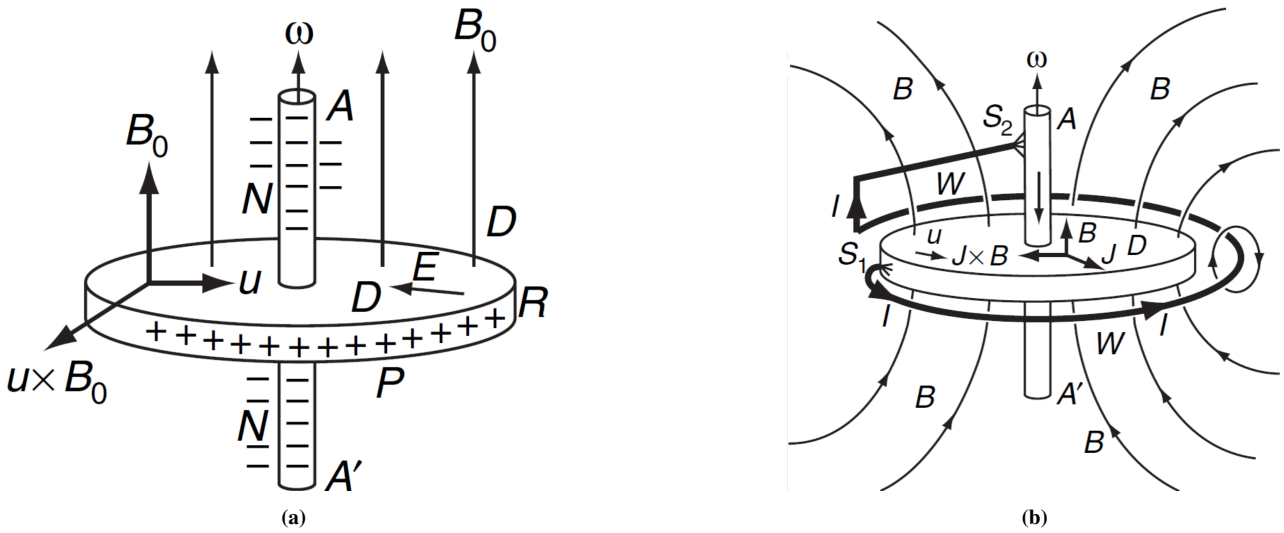

Figure 1: Illustration of the geodynamo mechanism with the simple case of a rotating and electrically conducting disk. **(a):** the disk is exposed to an external magnetic field $\mathbf{B}_0$, parallel to the angular velocity ω. The velocity due to rotation creates a motional emf, driving positive charge to the disk's rim, which in turn creates a stationary emf which cancel each other. Thus, no net electric current is generated. **(b):** idem as in case a, with the axis of rotation connected to the disk with a conducting wire from S_1 to S_2. The motional emf now drives the electric charge through the wire. The resulting current I generates the magnetic field $\mathbf{B}$ and the disk has become a dynamo. Courtesy of Roberts (2007).

from roughly 10 to 11 TW for the past ∼1.3 Gyr and propose the onset of the geodynamo to be in the range of 3.4-4 Ga. In the work of Aubert et al. (2009) an additional lower-end cooling model was proposed, where CMB flow increased linearly with age, from 3 TW to 11 TW since the Earth's formation. In more elaborate efforts, mantle convection has been reconstructed by incorporating past subduction locations and slabs which accumulate at the CMB. These reconstructions yielded a detailed evolution of CMB heat flow and showed that secular changes in Q_{cmb} have been as large as to 20% compared to a time average heat flow (Zhang and Zhong, 2011; Steinberger and Torsvik, 2012). Thus, estimates of the CMB heat flow and its evolution have been made; constraints on this dominant geodynamo boundary condition, however, are lacking.

The aim of this work is to improve our understanding of the CMB heat flux and its evolution. To that end, I propose numerical geodynamo models corresponding to varying types of CMB heat flux evolution. From those models I compute reversal frequencies which are compared with paleomagnetic observations to distinguish between plausible and less plausible modes of CMB heat flow evolution. By recreating past conditions of the geodynamo instead those of the mantle, especially puts new constraints on the evolution of the CMB heat flux.

First of all, the current state of capabilities of numerical geodynamo modelling is outlined in section 2, with that of modelling of reversals in particular. Section 3 concerns the installation of the code used to run the dynamo models. The methods and results of the geodynamo reconstruction are shown in sections 4 and 5; these results are discussed in section 6. Finally, a summary of the methods and findings of this work is given in section 7.

2. Rationale

The geodynamo mechanism can be clarified by regarding the simpler case of a rotating, electrically conducting disk (Fig. 1a). This disk is rotated at a constant angular velocity ω and is exposed to an external magnetic field $\mathbf{B}_0$. A general expression for the electromotive force (emf), i.e. the work done by the Lorentz force per unit charge along a closed path, is given by:

$$emf = \oint \left(\mathbf{E} + \mathbf{u} \times \mathbf{B}\right) \cdot \mathrm{d}\mathbf{l} \qquad (2)$$

where $\mathbf{E}$ and $\mathbf{B}$ are the electric and magnetic field respectively and $\mathbf{u} = \omega \times \mathbf{x}$ is the velocity of the conductor (e.g. Cook, 2002). This expression shows that rotating the disk generates an emf, proportional to $\mathbf{u} \times \mathbf{B}_0$, which is radially outward. Therefore, electric charge is driven radially outward and builts up at the disk rim (denoted by the '+'-symbols). From Eq. (2) we read that the emf is also proportional to $\mathbf{E}$, thus radially inward due to the charge buildup, such that the emf generated through rotation is eventually canceled. Therefore, in this situation of a rotating disk, the net electric current is zero (Roberts, 2007).

Let the disk be connected to the rotation axis with a conducting wire from location S_1 to S_2 (Fig. 1b). The emf due to rotation no longer creates a charge accumulation at the disk's rim, but an electric current I through the wire. According to the Biot-Savart law this current induces a secondary magnetic field $\mathbf{B}$ (see e.g. Fleisch, 2008). Therefore, when the disk is connected to the axis, kinetic energy is transformed into electric and magnetic energy - the disk has become a dynamo. As long as $\mathbf{B}$ is large enough to maintain the motional emf by itself, such a dynamo is addressed as a *self-exciting* dynamo. Although the geodynamo is more complex than the disk dynamo, e.g. due to different geometry, material properties and boundary conditions, it provides a first-order illustration of the generation of the geomagnetic field (Roberts, 2007).

2.1 Numerical geodynamo simulations

Numerical studies of the geodynamo have become increasingly popular over the last two decades. Unfortunately, inherent to such studies is the lack of computing power which prohibits the simulation of Earth-like dynamos. Therefore, the magnetic fields produced in these studies are strictly not equal to those of Earth. However, pioneering efforts have showed that certain properties of the geomagnetic field may be reproduced through numerical modelling (Glatzmaier and Roberts, 1995; Kageyama and Sato, 1995). This numerical success might be explained by regarding magnetic Reynolds number Rm, which provides a measure for the interactivity between the magnetic and velocity field (Christensen and Tilgner, 2004). In contrast to other parameters, Rm is modelled numerically with relatively good agreement to Earth-like values, that is $Rm \sim 10^3$ (Christensen and Wicht, 2007). In that light, the value of Rm is used as a criterion to assess whether a produced magnetic field is Earth-like (Christensen et al., 2010).

Another numerical succes is the reproduction of reversals (Glatz-

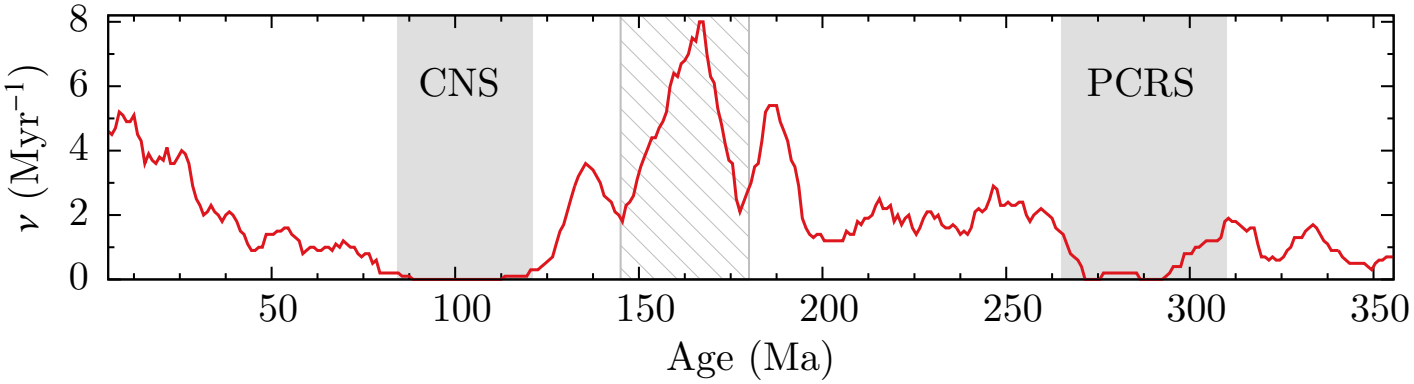

Figure 2: Secular changes in reversal frequency over the last 355 Myr, as obtained from marine magnetic and magnetostratigraphic data (Biggin et al., 2012). Gray areas represent tentative boundaries of superchrons, periods of time characterised by zero reversal frequency. The dashed area at 150-170 Ma denotes an period of high activity with relatively high reversal frequency, possibly up to 12 Myr^{-1}.

maier and Roberts, 1995). In terms of mathematics, reversals satisfy the equations that govern the geodynamo: prepending a minus sign to the magnetic field yields the same equations (e.g. Glatzmaier and Coe, 2007). However, physical understanding of reversal initiation is lacking. To provide insight in this matter empirically established relations between dynamo properties or *scaling laws* have been developed from large numbers of dynamo models, which may be extrapolated to Earth-like conditions. Such scaling laws provide insight into reversal initiation. For example, Christensen and Aubert (2006) proposed a relation between the relative dipole strength f_{dip} of a magnetic field and the modified Rossby number Ro_l, where the latter can be regarded as a measure for the mode of convection. More specifically, a large Ro_l corresponds to a convection regime characterised by a large amount of kinetic energy and/or small wavelength flow patterns. It is demonstrated that there is a distinct transition from a dipolar to non-dipolar magnetic field when Ro_l is increased beyond a critical value $Ro_{l,c} \approx 0.12$. This implies that the reversing nature of any dynamo is strongly controlled by Ro_l. An explanation for this behaviour is that a dipolar dynamo can not be sustained when inertial forces become large. It can be expected that viscous forces are indeed large for high Ro_l, such that a dipolar dynamo may break down correspondingly.

This relation between dipolarity and Ro_l was further investigated by Aubert et al. (2009) by incorporating models with varying ratio χ of the inner core boundary (ICB) radius to the core-mantle boundary (CMB) radius. They found that $Ro_{l,c}$ is dependent on χ and is in the range of 0.04-0.12, with χ between 0.01-0.35. Moreover, they observe that reversal frequency, increases with $|Ro_l - Ro_{l,c}|$. More recently, direct linear scaling laws between reversal frequency and Ro_l have also been established (Olson and Amit, 2014). Remarkably, the $Ro_{l,c}$ value is approximately 0.05 for all dynamo types, which corresponds to the findings of Aubert et al. (2009). Thus, these scaling laws demonstrate that reversal frequency is predominantly controlled by fluid flows and that there exists a critical mode of flow patterns which controls whether reversals occur or not

2.2 *Past reversal frequencies*

The occurrence of reversals is a stochastic process where some reversal related properties, such as chron and reversal duration, can be described by a Poisson distribution. This implies that reversals have no 'memory': one reversal is not influenced by its predecessor (Lhuillier et al., 2013). The duration of a superchron, i.e. a period of time of 10 Myr or larger during which no reversals occur, is comparable to the amount of time necessary for the mantle to perform a complete overturn. It was this observation that led to the concept that mantle convection, the geodynamo and geomagnetic field are related processes (Glatzmaier et al., 1999).

Marine magnetic and magnetostratigraphic data show that reversal frequency ν is time-dependent and has varied significantly over the last 355 Myr, with relative deviations from the time-averaged frequency $\delta\nu/\bar{\nu}$ up to $\sim$3 (Fig. 2) (Biggin et al., 2012). For example, no reversals occurred during the Cretaceous Normal Superchron (CNS), a period spanning almost 40 Myr (84-121 Ma). Also, the dipole moment was higher than average during the CNS, confirming the fact that reversal frequency and dipole moment are inversely related (Driscoll and Olson, 2011). In contrast, the period of approximately 150-170 Ma (Middle-Jurassic) was characterised by a low dipole moment and high reversal frequency - the latter having possibly been larger then 12 Myr^{-1} (Biggin et al., 2012). Another superchron within our period of interest, inferred from magnetostratigraphic data, is the PCRS (265-310 Ma). These main features of the reversal frequency history indicate what range of numerically produced frequencies would be realistic. In general, a zero reversal frequency during the CNS and PCRS and a high frequency at 150-170 Ma are expected.

Attempts have been made to reconstruct past features of Earth's magnetic field such as reversal frequency (Driscoll and Olson, 2009; Aubert et al., 2009; Olson et al., 2013). Such studies employ an estimate for the evolution of parameters that govern the geodynamo through time, for example secular changes in core-mantle boundary heat flow, inner core radius and rotation rate. The study done by Olson et al. (2013) in particular, not only imposed secular changes in global parameters, but also applied changes in the distribution of CMB heat flow, based on the CMB heat flow reconstruction by Zhang and Zhong (2011). Doing so, reversal frequencies produced in their models matched well with the reversal history from the geomagnetic polarity timescale (GPTS). For example, superchron-like conditions during times of the PCRS and relatively high frequencies during the middle Jurassic were reproduced. However, reconstructed reversal frequencies during the CNS were nonzero and in the order of magnitude of the present day value. In any case, previous works indicate that a reconstruction of the reversal frequency record can indeed be done through numerical modelling of the geodynamo.

3. Setup

In the numerical simulations I consider an electrically conducting fluid within a rotating spherical shell. The fluid consists of two components: a light and a heavy fraction, which is expressed in terms of light element mass percentage ξ. The shell has inner and outer radii r_{icb} and r_{cmb} respectively and rotates around the $\hat{\mathbf{z}}$-axis with a rotation rate Ω. Thermal and chemical perturbations from an isentropic (adiabatic) reference state are grouped within a single codensity variable C:

$$C = \alpha\rho T' + \Delta\rho\xi' \tag{3}$$

where T is temperature, α is the thermal expansion coefficient, ρ is the mass density, $\Delta\rho$ is the mass density difference between the light and heavy fraction and the primes denote absolute deviations from the reference state (Braginsky and Roberts, 1995). The use of the co-density formulation and applying the Boussinesq approximation allow the equations governing the geodynamo to be written in the following nondimensional form:

$$\frac{\partial \mathbf{u}}{\partial t} + \mathbf{u}\cdot\nabla\mathbf{u} + 2\hat{\mathbf{z}}\times\mathbf{u} + \nabla P = Ra_Q \frac{\mathbf{r}}{r_{\mathrm{cmb}}} C + (\nabla\times\mathbf{B})\times\mathbf{B} + E\nabla^2\mathbf{u} \tag{4}$$

$$\frac{\partial \mathbf{B}}{\partial t} = \nabla\times(\mathbf{u}\times\mathbf{B}) + \frac{E}{Pm}\nabla^2\mathbf{B} \tag{5}$$

$$\frac{\partial C}{\partial t} + \mathbf{u}\cdot\nabla C = \frac{E}{Pr}\nabla^2 C + S_{T/\xi} \tag{6}$$

$$\nabla\cdot\mathbf{u} = 0 \tag{7}$$

$$\nabla\cdot\mathbf{B} = 0 \tag{8}$$

where $\mathbf{u}$ is fluid velocity and P is pressure (Aubert et al., 2009). Equations (4) to (8) are the equations representing conservation of momentum, magnetic induction, heat transport, the incompressibility of the fluid and the solenoidality of the magnetic field respectively. These equations are cast in nondimensional form, giving rise to the nondimensional parameters:

$$E = \frac{\nu}{\Omega D^2} \tag{9}$$

$$Pr = \frac{\nu}{\kappa} \tag{10}$$

$$Pm = \frac{\nu}{\lambda} \tag{11}$$

$$Ra_Q = \frac{g_{\mathrm{cmb}} F}{4\pi\rho\Omega^3 D^4} \tag{12}$$

which are the Ekman, Prandtl, magnetic Prandtl and Rayleigh number respectively, where ν, κ and λ are the viscous, thermal/chemical and magnetic diffusivity, $D = r_{\mathrm{cmb}} - r_{\mathrm{icb}}$ is the shell thickness and g_{cmb} is the gravity field magnitude at the CMB. Moreover, time has been scaled to the period of rotation Ω^{-1}, length to D, velocity to $D\Omega$ and the magnetic field to $\sqrt{\rho\mu}D\Omega$, with μ the magnetic permeability (Aubert et al., 2009). A table with all used symbols and abbreviations is given in appendix A.3.

The variable $F = F_{\mathrm{icb}} + F_{\mathrm{cmb}}$ is the sum of the mass anomaly fluxes through the inner core boundary (ICB) and CMB, with

$$F_{\mathrm{icb}} = -\int_{\Sigma_{\mathrm{icb}}} \kappa\nabla C\cdot\mathrm{d}\mathbf{S} \tag{13}$$

and

$$F_{\mathrm{cmb}} = -\int_{\Sigma_{\mathrm{cmb}}} \kappa\nabla C\cdot\mathrm{d}\mathbf{S} \tag{14}$$

where Σ_{icb} and Σ_{cmb} are the ICB and CMB surface respectively. Assuming no chemical flux through the CMB, the latter may be written as:

$$\begin{aligned} F_{\mathrm{cmb}} &= -\int_{\Sigma_{\mathrm{cmb}}} \kappa\nabla(\alpha\rho T')\cdot\mathrm{d}\mathbf{S} \\ &\simeq -\int_{\Sigma_{\mathrm{cmb}}} \kappa\alpha\rho\nabla(T - T_{\mathrm{ad}})\cdot\mathrm{d}\mathbf{S} \\ &\simeq \frac{\alpha}{c_P}(Q_{\mathrm{cmb}} - Q_{\mathrm{cmb,ad}}) \end{aligned} \tag{15}$$

where uniformity of material properties across the CMB is assumed and Fourier's law for thermal conduction is applied. The variable c_P denotes the heat capacity and the 'ad' subscript denotes quantities along the outer core adiabat. Thus, from Eq. (15) we read that F may be expressed in terms of the total CMB heat flux. Finally, the last term in Eq. (6) is expressed as:

$$S_{T/\xi} = 3\,\frac{1 - 2F_{\mathrm{icb}}/F}{r_{\mathrm{icb}}^3 - r_{\mathrm{cmb}}^3} \tag{16}$$

3.1 Benchmark and strong scaling

The governing equations (4) to (8) were solved numerically by means of the PARODY-JA code (e.g. Aubert et al., 2009). The code was not set up at our institute prior to this work. Therefore I made use of the benchmark study by Christensen et al. (2001), to ensure the correct installation of PARODY-JA. Their study consists of three benchmark cases, case 0 to 2, of which the former considers purely thermal convection. Therefore, only cases 1 and 2 were considered in this benchmark for which a reproduction of the results presented by Christensen et al. (2001) was made.

Case 1 considers magnetoconvection where both boundaries have no slip conditions and are electrically insulating. A fixed nondimensional temperature contrast across the shell $\Delta T = 1$ was used as thermal boundary condition. Quantities tested in this case are the outer core volume averaged kinetic and magnetic energy, $\langle E_{\mathrm{kin}}\rangle$ and $\langle E_{\mathrm{mag}}\rangle$, respectively, the radial magnetic field B_r at the CMB and velocity field u_r at shell half-depth. Moreover, I consider the poloidal component of the magnetic field B_θ at half-depth, the equator and at the location for which the conditions $u_r = 0$ and $\partial u_r/\partial r > 0$ are valid.

Case 2 is identical to case 1, except it has a conducting and freely rotating inner core with magnetic permeability and electric conductivity equal to that of the outer core. For this case, the average energies of case 1 were computed and additionally the inner core volume average magnetic energy $\langle E_{\mathrm{mag,ic}}\rangle$ and rotation rate ω_{ic}. Both cases employ $\chi = 0.35$ and a lateral spherical harmonic decomposition up to degree and order 44. In case 1, 200 radial nodal points were used; in case 2, 120 were used of which 25 in the inner core. Values of the governing parameters (Eq. (9)-(11)) for both cases are listed in Table 1. It must be noted that in the work of Christensen et al. (2001) a different nondimensionalisation is applied to the governing equations, such that their Rayleigh number Ra is written in terms ΔT, instead of a bouyancy flux as is the case in Eq. (12):

$$Ra = \frac{\alpha g_{\mathrm{cmb}}\Delta T D}{\nu\Omega} \tag{17}$$

For the initial conditions of the benchmark models the reader is referred to Christensen et al. (2001). Lastly, the following symmetries in the solutions are assumed: single symmetry about the equator and fourfold longitudinal symmetry.

The efficiency of the PARODY-JA parallelisation on our system was also investigated. To that end, a strong scaling test is performed: the benchmark case 1 has been run with a varying number of processors and for each model run the amount of time necessary to perform 10^5 time iterations was determined. This process has been repeated for a different number of radial nodal points.

Parameter	Case 1	Case 2
Ra	100	110
E	10^{-3}	10^{-3}
Pr	1	1
Pm	5	5

Table 1: The values of the governing parameters given by Eq. (9)-(11) and (17) used in the benchmark cases 1 and 2 (Christensen et al., 2001).

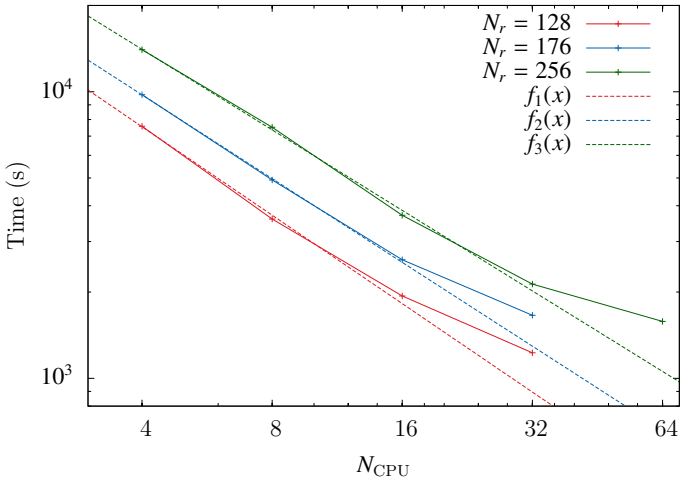

Figure 3: The time necessary to perform the case 1 benchmark versus the number of processors used for varying radial resolution. The power law fits to the computing time are shown as dashed curves (Table 2). The fits show that a doubling of N_{CPU} halves the computing time. The power law fits break down when N_{CPU} is increased beyond a critical value, which increases with N_r.

i	N_r	α_i (10^4)	β_i
1	128	31.3 ± 2.6	-1.03 ± 0.03
2	176	37.5 ± 1.1	-0.97 ± 0.02
3	256	51.3 ± 2.9	-0.93 ± 0.05

Table 2: The coefficients α_i and β_i from the power law fits of the computing time versus N_{CPU} for varying N_r. For all N_r $\beta_i \approx -1$, showing a reciprocal relationship between computing time and N_{CPU}. The coefficient α_i increases with N_r, displaying the fact that computing time is a function of radial resolution.

Finally, power law fits of the form $f_i = \alpha_i x^{\beta_i}$ were made to computing time versus the number of processors used for all radial nodal point configurations.

3.2 Results

The quantities $\langle E_{\mathrm{kin}} \rangle$ and $\langle E_{\mathrm{mag}} \rangle$ of the case 1 benchmark initially show oscillatory behaviour, of which amplitudes decay with time (Fig. 5a). At $t/\tau_v \approx 6$ they converged to the benchmark values within the margin of uncertainty. In total, case 1 was run for roughly 8 hours. The poloidal component of the magnetic field B_θ converged to a value of $B_\theta = -4.9576$. This value is slightly outside the uncertainty of the reference value of -4.9289 ± 0.0060, corresponding to a relative error of approximately 0.6%. The final radial magnetic field B_r and radial velocity u_r on the CMB and shell half depth respectively are shown in Fig. 4. The distributions are identical to the ones given in Christensen et al. (2001) (Fig. 1 in their notation), including the pattern of equatorial symmetry and quadruple longitudinal symmetry.

Similar to case 1, all quantities tested for the case 2 benchmark converge towards the reference values, with a total run time of 4 hours (Fig. 5b). However, the quantities $\langle E_{\mathrm{mag}} \rangle$ and ω_{ic} do so slightly outside the given uncertainty margins. For these quantities the relative error to the reference values is in the order of 0.1%. Thus, in both benchmark cases all quantities either converge within the margin of uncertainty or eventually show a small error. Therefore, the benchmark is deemed successful and it is accepted that PARODY-JA is installed correctly.

The strong scaling results and corresponding power law fits f_i are given in Fig. 3. The power law fit coefficients are given in Table 2. For all fits $\beta_i \approx -1$, so that computing time has a reciprocal dependency on N_{CPU}. This implies that a doubling of N_{CPU} yields a decrease in computing time of a factor two. Also, the coefficient α_i increases with N_r, thus the computing time increases with resolution. From Fig. 3 the reciprocal dependency can be seen to break down at a critical value $N_{\mathrm{CPU,crit}}$. For example, $N_{\mathrm{CPU,crit}} \approx 32$ for $N_r = 128$ and can be seen to increase with N_r. Therefore, for low resolution runs (N_r smaller than e.g. 50) 8 CPUs should be employed at most. In any case, the strong scaling shows that the PARODY-JA speedup with increasing N_{CPU} is satisfactory.

4. The initial model

Reconstructing features of the geodynamo required estimates of its control parameters during past times. To make such estimates the approach of Olson et al. (2013) was adopted, which consists of the following steps:

i. A combination of parameters is chosen which yield a dynamo representative of the present-day geodynamo. This work considers reversal frequency an important aspect of the geodynamo, therefore this dynamo model should produce the present-day frequency of $\sim$4 Myr^{-1} (Biggin et al., 2012). Various dynamos are tested by varying Ra_Q and keeping all other control parameters fixed. The dynamo which yields a frequency in closest agreement with 4 Myr^{-1} will be referred to as the *initial model*.

ii. An estimate is made of secular changes in the governing parameters at specific times, with respect to the present day. In this study secular changes in the following parameters are considered: Ra_Q (therefore Q_{cmb}), E, χ, F_{icb}/F and δq. For example, if at a specific time Ra_Q is estimated to be smaller than the present-day value by a factor two, such a secular change is noted as $Ra_Q(t)/Ra_Q(0) = 0.5$.

iii. The secular changes in the control parameters are applied to those of the initial model. Then, for the times corresponding to the applied changes, numerical models of the geodynamo can be run. At those times features such as reversal frequency can be computed from the model run results.

An upside to this approach is that the estimated governing parameters and the changes therein are computationally manageable, such that geodynamo evolution can in fact be modelled numerically with the available computing power. However, this method is heavily dependent on the choice for the initial model and it is debatable whether the chosen initial model is representative for the present-day geodynamo (Olson et al., 2013). Also, determining the initial model is nontrivial. For example, the set of parameters which reproduce the present-day reversal frequency is non-unique, so that a choice the most Earth-like initial model must be made. Moreover, the occurence of reversals is random, implying that the absence of reversals during a particular model run, might be incidental. Vice versa, the occurrence of a large number of reversals might not might be a representative feature of the model, but merely coincidental. Moreover, caution should be taken with the fact that this method assumes that Earth-like changes in the governing parameters, estimated in step ii., may be applied to the not Earth-like initial model directly.

For the initial model I set the values $E = 3 \cdot 10^{-4}$, $Pr = 1$, $\chi = 0.351$ (Aubert et al., 2009). To prevent dynamo failure due to Pm being too small it is set at a reliable value of $Pm = 20$ (Christensen and Aubert, 2006). Core-mantle boundary heat flow data by (Biggin et al., 2012)

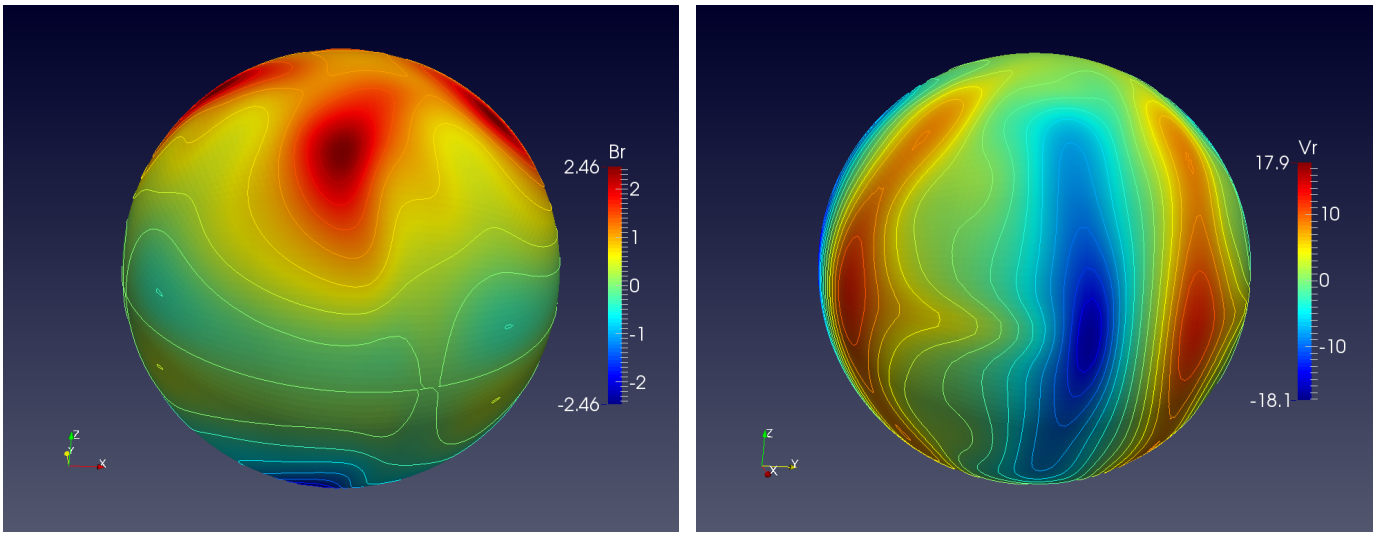

(a) **(b)**

Figure 4: The radial magnetic at the CMB (a) and radial velocity field at shell half-depth (b) for the case 1 benchmark. The distributions strongly match those by Christensen et al. (2001) (Fig. 1 in their notation). The symmetry about the equator and the fourfold longitudal symmetry of the solutions is noticable.

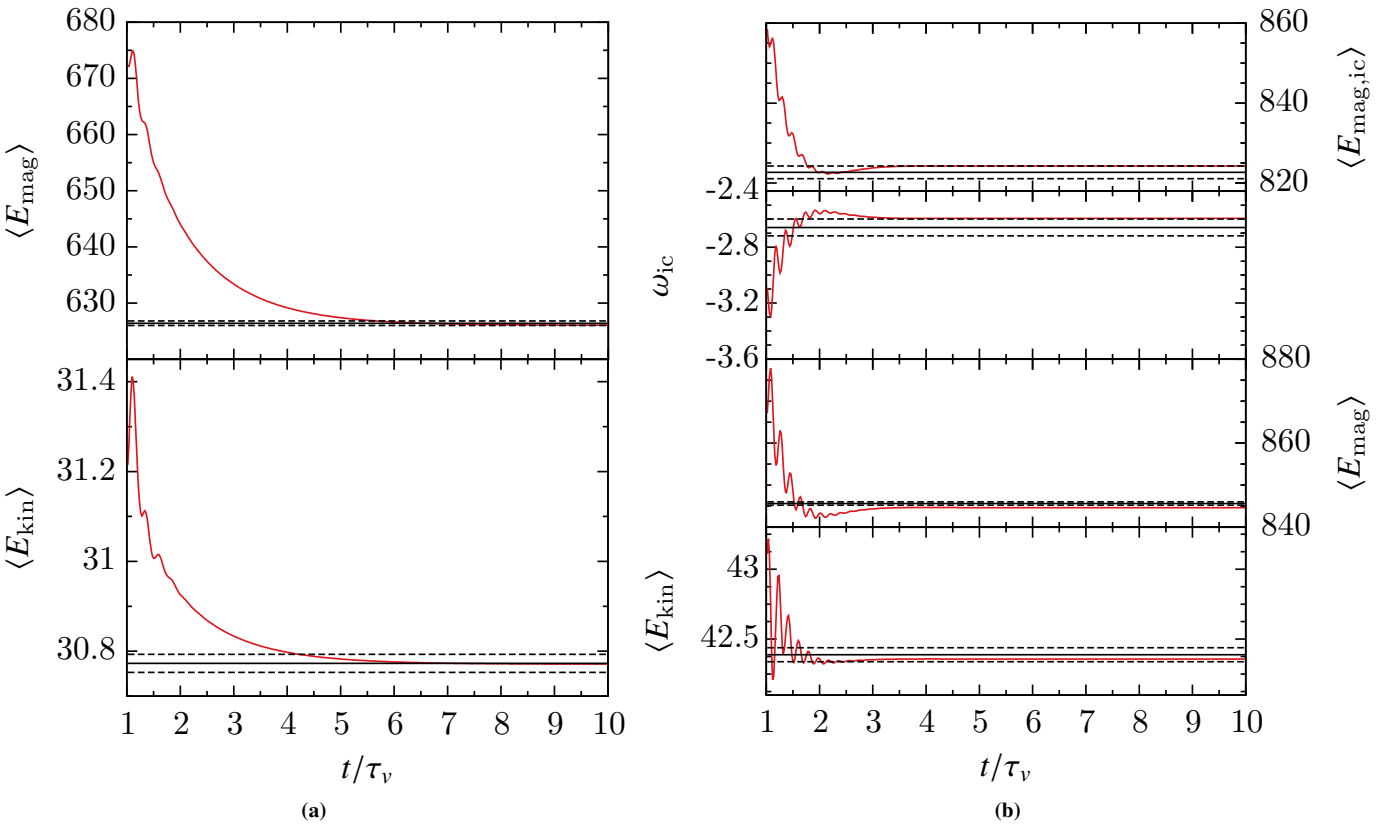

(a) **(b)**

Figure 5: Tested quantities in the benchmark cases 1 and 2 as function of time (red lines, a and b respectively). The solid and dashed black lines are the reference values and corresponding uncertainties respectively (Christensen et al., 2001). For case 1, the computed quantities converge to the benchmark values within the uncertainties. For case 2, only $\langle E_{\rm kin} \rangle$ and $\langle E_{\rm mag,ic} \rangle$ converge within the uncertainties, though for all quantities the final relative error to the benchmark values is approximately 0.1%.

is employed, yielding $\delta q = 1.8$. The governing equations (4)-(8) are solved with 40 radial nodal points, a lateral spherical harmonic decomposition of maximum degree and order 32 and 8 CPUs. The same boundary conditions are used as in benchmark case 1, though instead of a fixed temperature contrast I impose a ICB mass anomaly flux to total mass flux ratio $F_{\rm icb}/F = 0.5$ and set Ra_Q. The Ra_Q is varied between candidate models between the range of $1.00 \cdot 10^{-4}$ and $1.35 \cdot 10^{-4}$. For all initial models Rm is computed through a scaling law extrapolation described further on in section 5.1.

4.1 Computing reversal frequency

During a dynamo model run, the magnetic dipole colatitude $\theta_{\rm dip}$ fluctuates as a function of time, potentially in the form of reversals. To count the number of reversals $N_{\rm rev}$ during a model run, the algorithm proposed by Lhuillier et al. (2013) is adopted. It must be noted that instead of dipole moment the norm of the degree one, order zero Gauss coefficient $|g_1^0|$ is used as a measure of the dipole strength of the magnetic field. The method we employ is based on the following steps:

i. For a model run, the time-average of $|g_1^0|$ and corresponding standard deviation, $\mu_{|g_1^0|}$ and $\sigma_{|g_1^0|}$ respectively, are computed.

ii. A period of time for which $|g_1^0| < \mu_{|g_1^0|} - \sigma_{|g_1^0|}$ is counted as a low intensity event (LIE).

iii. The LIE is classified as a stable LIE (SLIE), reversal or failed reversal. If, during any LIE, the dipole colatitude did not cross the equator, the LIE was classified as a stable SLIE. Alternatively, if it did cross the equator during that period, but was in the same hemisphere as when the LIE initiated, the LIE was classified as a failed reversal. Lastly, if the dipole colatitude crossed the equator and was in the other hemisphere as the initial colatitude the LIE was counted as a reveral (Lhuillier et al., 2013).

This methodology is employed in the *Reversal Detector*[1] software of which the source code is given in appendix A.2.

Once $N_{\rm rev}$ was determined for a model run, the corresponding reversal frequency was computed through $\nu = N_{\rm rev}/\tau_r$, with τ_r the total time over which the model was run. Like all quantities, time is nondimensional within PARODY-JA calculations and is given in terms of viscous time $\tau_{\rm v}$ in its output. Therefore, the reversal frequency computed by the method above is also nondimensional, that is in terms of inverse viscous times $\tau_{\rm v}^{-1}$. However, we are interested in dimensional reversal frequencies as we aim to compare our frequencies with those in the reversal frequency record. Therefore, we dimensionalise the reversal frequency by assuming the relation $Pm\,\tau_{\rm v} \simeq \tau_\lambda$ where $\tau_\lambda \approx 2 \cdot 10^5$ yr is the magnetic diffusion time (Olson et al., 2012). It follows then that, as we consider $Pm = 20$, that $\tau_{\rm v} \approx 10^4$ yr and that ν is computed in units of 10^{-4} yr $^{-1}$.

4.2 Results

Seven models potential initial model were obtained, referred to as the *candidate models* (Table 3). In general, the number of LIEs and reversals counted during a model run, $N_{\rm LIE}$ and $N_{\rm rev}$ respectively, increase with Ra_Q. An exception to this trend are the models e. and g., with $Ra_Q = 1.22 \cdot 10^{-4}$ and $Ra_Q = 1.35 \cdot 10^{-4}$ respectively, which show an anomalously large reversal frequency of an order of magnitude larger compared to the other candidates. Also, in these two models $\mu_{|g_1^0|}$ is relatively low, which suggests that the dipolar component of the magnetic field is too weak to sustain a stable polarity. In contrast to other parameters, $\sigma_{|g_1^0|}$ shows less variability among the candidate models with $\sigma_{|g_1^0|} \approx 0.2$, with the exception of candidate a. Therefore, it appears that dipolar component of the magnetic field, fluctuates within a fixed range.

[1] Available upon request

In Fig. 6 time sequences of $\theta_{\rm dip}$ and $|g_1^0|$ of the candidate models are shown. The most stable model (in terms of polarity) and that with the strongest dipole component, is displayed in Fig. 6a, in which no equator crossings of $\theta_{\rm dip}$ are found. In Fig. 6b to 6g, the number of equator crossings and the number of LIEs is found to increase with Ra_Q, while the duration of LIEs decreases. Exceptions are again the weakly dipolar models e. and g., which show relatively long periods at which $|g_1^0|$ is low, ranging from approximately 20 to 50 $t/\tau_{\rm v}$. The fact that these two models are relatively unstable, even though the Ra_Q is not anomalously high, shows that Ra_Q is not the only factor controlling dipole stability and the occurence of reversals. This is also illustrated by the fact that even though Ra_Q is higher in model c. compared to b., no reversals occurred in model c. Therefore, reversal frequency might not be scaled accurately to Ra_Q and Ro_l might indeed be a better quantity to construct a scaling law for reversal frequency (Olson and Amit, 2014). Model f. yields a reversal frequency closest in agreement with the present-day value of 4 Myr^{-1} and is chosen as our intitial model.

5. Geodynamo evolution

To reconstruct past features of the geodynamo secular changes in the parameters Ra_Q, E, χ, $F_{\rm icb}/F$ and δq were taken in consideration. Changes in E and χ were obtained from (Olson et al., 2013) and are based on length-of-day variations by Williams (2000) and the core thermal evolution proposed by Labrosse et al. (2007) respectively. An estimate for the secular evolution of Ra_Q was made by writing it in terms of E:

$$Ra_Q = \frac{g_{\rm cmb} F E^3 D^2}{4\pi\rho\nu^3} \tag{18}$$

Then, secular changes in the Rayleigh number, $Ra_Q(t)/Ra_Q(0)$ may be expressed as:

$$\frac{Ra_Q(t)}{Ra_Q(0)} \simeq \frac{F(t)}{F(0)} \left(\frac{E(t)}{E(0)}\right)^3 \left(\frac{1-\chi(t)}{1-\chi(0)}\right)^2 \tag{19}$$

under the assumption that ρ, ν, $r_{\rm cmb}$, $r_{\rm cmb}$ and $g_{\rm cmb}$ are constant within the time interval of our reconstruction. This expression requires estimates for the secular variations in total mass anomaly flux $F(t)/F(0)$. One may do so in terms of contributions from the ICB and CMB through subtitution of Eq. (15), yielding:

$$\frac{F(t)}{F(0)} \simeq \frac{F_{\rm icb}(t) + \frac{\alpha}{c_P}(Q_{\rm cmb}(t) - Q_{\rm ad})}{F_{\rm icb}(0) + \frac{\alpha}{c_P}(Q_{\rm cmb}(0) - Q_{\rm ad})} \tag{20}$$

where the $Q_{\rm ad}$ is set at 6 TW and assumed constant (Aubert et al., 2009). Under the Boussinesq approximation one may express the ICB mass anomaly flux in terms of that through the CMB. In that light, the following relation is used (Aubert et al., 2009):

$$\Phi_{\rm icb} + \Phi_{\rm cmb} = F_{\rm icb}(\psi_{\rm icb} - \bar{\psi}) - F_{\rm cmb}(\psi_{\rm cmb} - \bar{\psi}) \tag{21}$$

where $\Phi_{\rm cmb}$ and $\psi_{\rm cmb}$ denote the energetic dissipation and gravitational potential at the CMB (idem for the ICB subscript) and $\bar{\psi}$ is the depth average gravitational potential (Buffett et al., 1996). As the gravitational potential is gravitational energy per mass, the relation above shows how a mass anomaly flux may be translated to an energy flux. It also shows that if the boundary dissipations and the gravitational potentials are known, $F_{\rm icb}$ can be estimated from $F_{\rm cmb}$ (Thus $Q_{\rm cmb}$). The boundary dissipations and gravitational potentials at the boundaries were computed at eacht timestep, using the expressions given by Aubert et al. (2009). Then, using a given a total CMB heat flow at a certain time, the corresponding ICB mass anomaly flux can be computed and with that

Label	Ra_Q (10^{-4})	Rm	$\mu_{\lvert g_1^0\rvert}$	$\sigma_{\lvert g_1^0\rvert}$	N_{LIE}	N_{rev}	τ_r	ν (Myr^{-1})
a.	1.00	780	0.55	0.12	37	0	81	0
b.	1.10	835	0.43	0.21	36	2	191	1.04
c.	1.13	857	0.48	0.19	38	0	123	0
d.	1.17	871	0.36	0.22	172	10	350	2.86
e.	1.22	934	0.25	0.21	444	74	334	22.2
f	**1.26**	**1029**	**0.32**	**0.22**	**192**	**11**	**286**	**3.85**
g	1.35	984	0.24	0.21	147	22	110	19.9

Table 3: List of characteristic quantities of the candidate models. In general, N_{LIE}, N_{rev} and ν increase with Ra_Q, for the range tested. The candidates e. and g. show an anomalously high ν and small $|g_1^0|$. For all models except the one for $Ra_Q = 1.00 \cdot 10^{-4}$, $\sigma_{|g_1^0|} \approx 0.2$. The model with $Ra_Q = 1.26 \cdot 10^{-4}$ is characterised by a reversal frequency which best matched the present-day value of 4 Myr^{-1} among the models tested and is our initial model (printed bold).

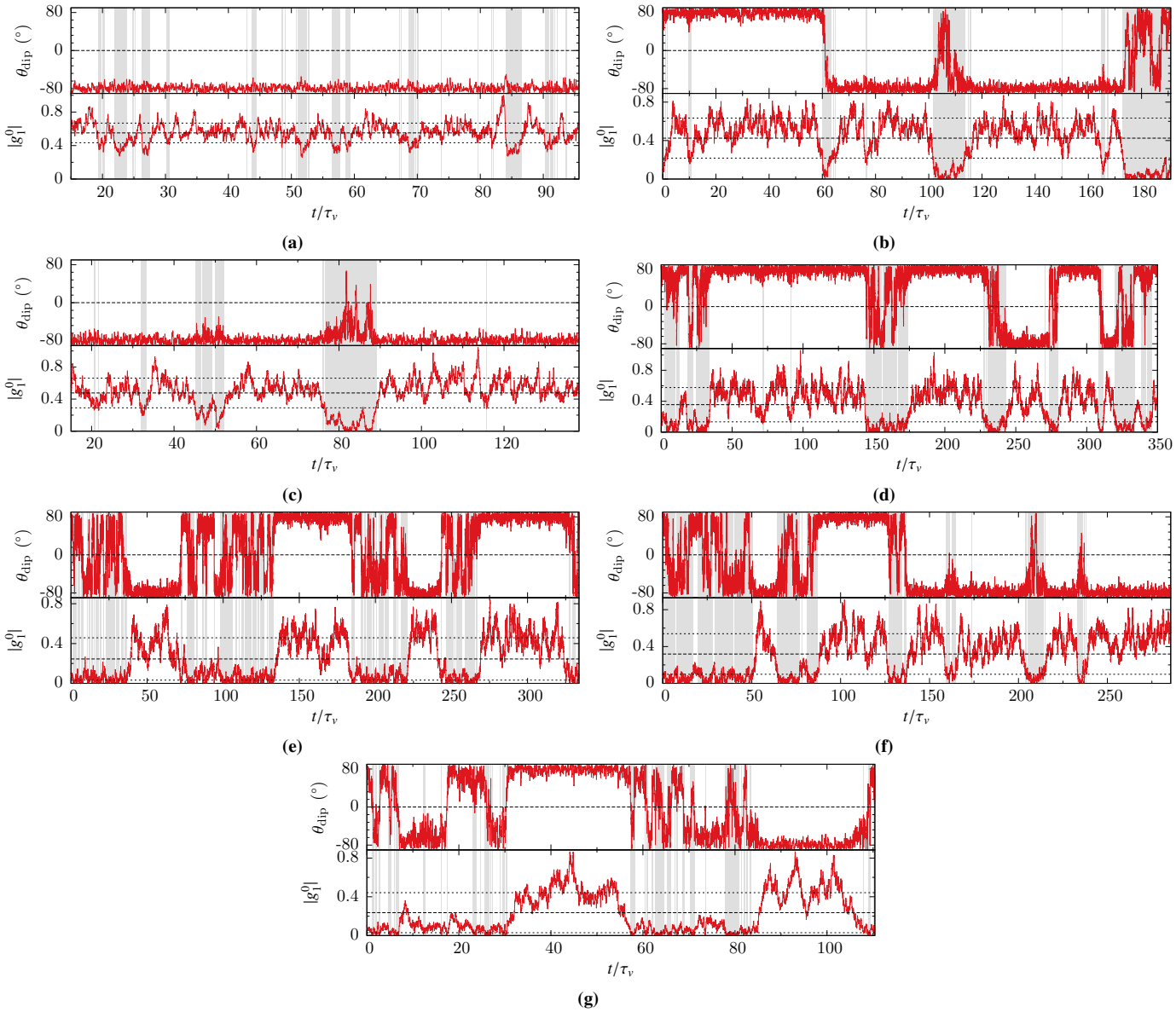

Figure 6: Time sequences of θ_{dip} and $|g_1^0|$ (top and bottom respectively) for the candidate models, where labelling of the figure corresponds to that of Table 3. The dashed line in the bottom figure shows $\mu_{|g_1^0|}$; dotted lines are $\mu_{|g_1^0|} \pm \sigma_{|g_1^0|}$. Gray areas correspond to LIEs, i.e. periods of time for wich $|g_1^0| < \mu_{|g_1^0|}$, as obtained with the Reversal Detector. For the models a. and c., early changes have been omitted as these were predominantly due to the equilibration of the dynamo. Model a. shows the most stable behaviour with θ_{dip} not crossing the equator at any time. For higher Ra_Q, the number of times the θ_{dip} passes the equator can be seen to increase. The most reversals can be found in the anomalously unstable models e. and g., which are characterised by relatively long periods at which $|g_1^0|$, some spanning more than $40t/\tau_v$. The number and duration of LIEs and generally increase and decrease respectively, with Ra_Q. The shortest LIEs are found in models e. and g., in which the magnetic field is the least dipolar among the candidate models.

the change in the Rayleigh number. Lastly, the evolution of the ratio F_{icb}/F was estimated by assuming the proportionality:

$$\frac{F_{\mathrm{icb}}}{F} \propto \Sigma_{\mathrm{icb}} \tag{22}$$

So that we find the following expression for changes in this ratio:

$$\begin{aligned}\frac{(F_{\mathrm{icb}}/F)(t)}{(F_{\mathrm{icb}}/F)(0)} &= \left(\frac{r_{\mathrm{icb}}(t)}{r_{\mathrm{icb}}(0)}\right)^2 \\ &= \left(\frac{\chi(t)}{\chi(0)}\right)^2 \end{aligned} \tag{23}$$

5.1 Computation of additional quantities

In the core evolution series we compute the modified Rossby number Ro_l and magnetic Reynolds number Rm at each timestep. The former is obtained by using the scaling law:

$$Ro_l = 0.54\, p^{0.48} E^{-0.32} Pr^{0.19} Pm^{-0.19} (1+\chi) \tag{24}$$

where p is a nondimensional measure for convective power and is an output parameter of PARODY-JA (Aubert et al., 2009). From the definition of Ro_l the regular Rossby number can be computed:

$$Ro = \frac{\pi}{\bar{l}_u} Ro_l \tag{25}$$

where $\bar{l}_u$ is the mean spherical harmonic degree of fluid flow, also a PARODY-JA output parameter (Christensen and Aubert, 2006). From Eq. (24) and (25) we can then compute Rm:

$$Rm = \frac{Ro}{E_\lambda} \tag{26}$$

where $E_\lambda = E/Pm$ is the magnetic Ekman number.

Unfortunately, we will see that the reversal frequencies for the core evolution series are unrealistic, being two orders of magnitude too high. Therefore, reversal frequencies ν' are computed using the scaling law obtained by (Olson and Amit, 2014) in addition to the ones from the Reversal Detector (see section 4.1). In their work, a number of scaling laws are proposed for various types of CMB heat flow distributions. I apply the scaling law designed for dynamos with a CMB heat flow distribution resembling wave velocity at the CMB as from seismic tomography, which is tested for varying δq (scaling law T(δq) vs. Ro_l' in their notation). It is given by:

$$\nu' = 8.19\, Ro_l\,(1+\delta q/2) - 0.42 \tag{27}$$

Note that this relation yields a nondimensional frequency. Therefore, ν' is dimensionalised by dividing it by the magnetic diffusion time $\tau_\lambda \approx 2\cdot 10^5$ yr (Olson and Amit, 2014).

5.2 CMB heat flow evolution

The analysis given above leaves one unknown: knowledge of the CMB heat flow during the time of reconstruction. Therefore, the mantle convection reconstruction model by Steinberger and Torsvik (2012) is applied, henceforward referred to as ST12. It is based on the subduction proposed in (Steinberger and Torsvik, 2010) and is computed through spectral methods and employes a depth dependent viscosity profile and a chemically distinct layer at the base of the mantle. Following the notation of Biggin et al. (2012) we use the case 2a variation of ST12, which is identical to ST12 except that it is run 100 Myr extra before the reconstruction (without subduction), such that the system has equilibrated and a basal thermal boundary layer has formed. For more details on the ST12 model the reader is referred to Biggin et al. (2012) and Steinberger and Torsvik (2012).

The total CMB heat flow Q_{cmb} as a function of time as from ST12 is shown in Fig. 8; sample heat flow distributions from ST12 at various times are shown in Fig. 7. The CMB heat flow distributions used are truncated at spherical harmonic degree and order 8. The core evolution series employing the CMB heat flow evolution as from ST12 is referred to as the CE series. As we will see, the CE series yielded undesirable results, characterised by models with unrealistic reversal frequencies and dynamo failure. Therefore, other series are run in better agreement with the observed record and which provide insight in the non-Earth-like character of the CE series. We run series in which fluctuations from the time average Q_{cmb} are damped by a factor 2 (CEd), Q_{cmb} is described by a linear increase with time (CEl) and one with that linear increase and a constant E (CEe) (Fig. 8).

PARODY-JA accepts CMB heat flow distributions in the form of spherical harmonics only. Spherical harmonics come in various conventions and the convention adopted in the data was not consistent with the one applied within PARODY-JA. Therefore, to impose any CMB heat flow distribution, a convention conversion was made. To be more precise, a non-trivial conversion was done from tesseral or real-values spherical harmonic coefficients to complex-valued ones. This mathematical operation is described in appendix A.1.

5.3 Results

For the CE series ν shows a discrepancy between the reversal record of two orders of magnitude (Table 4). The ν' frequencies of the CE series are also too high, having the largest deviation from the observations among all core evolution series (Fig. 9). They do, however, perform better than the ν frequencies, showing a discrepancy of a single order of magnitude. Dynamos for ages 150 Ma and beyond fail, i.e. those combinations of governing parameters do not yield a dynamo solution, such that these models do not yield usable results. For the CE series Rm is well above the minimum value required for an Earth-like dynamo and Ro_l is of a typical magnitude at which reversals occur (Christensen and Aubert, 2006; Christensen et al., 2010; Olson and Amit, 2014). At 50 Ma and 90 Ma Rm and Ro_l are large compared to other core evolution series, with Rm being twice as large as a typical value for the candidate models (Table 3). This indicates that flow velocity is sufficiently high to deform the magnetic field such that a dipolar state can not be sustained, which might explainin the high reversal frequencies.

In terms of ν' frequencies the CEd series perform significantly better than the CE series, with ν' in the same order of magnitude as the observations. The misfit to the observations is still considerable, with the largest frequency of the series at 90 Ma for which a (near) zero frequency is observed. This relatively large frequency coincides with the fact that in the ST12 model Q_{cmb} peaks at approximately 90 Ma (Fig. 8). In contrast to the CE series, Ro_l decreases gradually with age in the CEd series, indicating that convection currents decreases and/or occurs at larger wavelengths. Even though the CEd is more realistic compared to CE, dynamo failure still occurs during the second half of the reconstruction.

The results of the CEl series are similar to the CEd series. For both series ν' is comparable at ages 100 Ma and earlier, and Ro_l and Rm show the same trends with age. Also, Rm is lower than in the CEd series, and therefore in better agreement with the candidate models. The CEl series improves the fit to the observations with a non-failing dynamo at 180 Ma. At that time, ν' shows the best fit among reversal frequencies computed in all series.

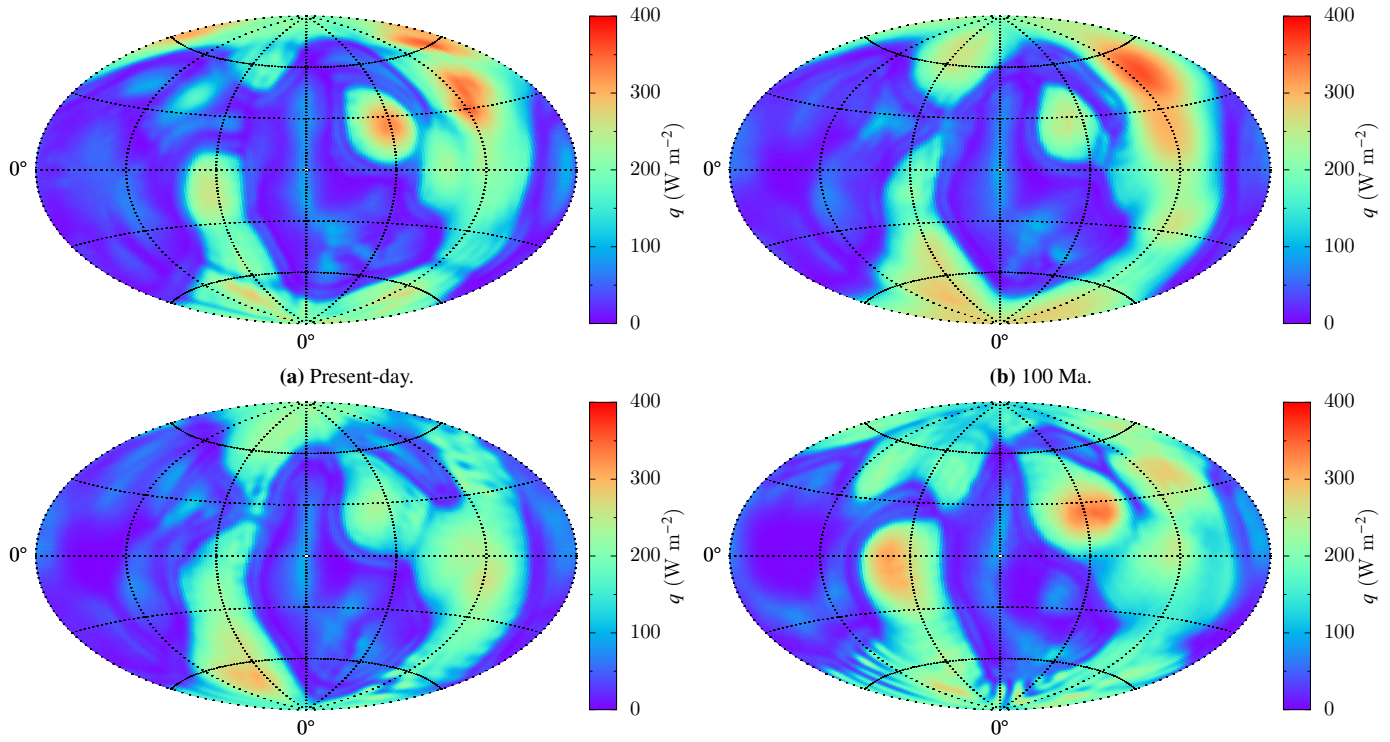

(a) Present-day. **(b)** 100 Ma. **(c)** 150 Ma. **(d)** 270 Ma.

Figure 7: Aitoff projection of the CMB heat flow distribution from the the ST12 model at selected times (modified from (Biggin et al., 2012)). At all times the distributions consist of a dominant spherical harmonic degree two, order zero component, corresponding to the distribution of Large Low Shear Velocity Provinces (LLSVPs) beneath Africa and the Pacific Ocean (Steinberger and Torsvik, 2012).

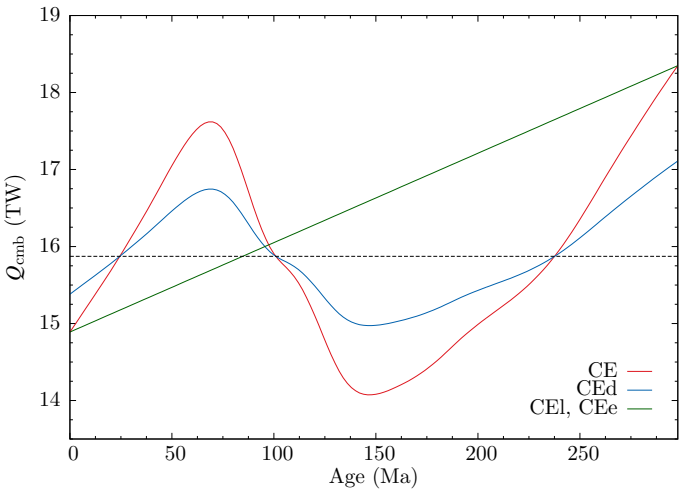

Figure 8: The heat flow magnitude evolution scenarios used in the core evolution series. The CE series employs the evolution of Q_{cmb} as in the ST12 mantle reconstruction model (Steinberger and Torsvik, 2012); the CEd series employ the same data with the exception that the secular changes in Q_{cmb} with respect to the time average (dashed line) are halved. The CEl and CEe incorporate a linear increase in Q_{cmb}, using the initial and final values as from the CE(d) series.

The CEe series has the largest success rate among all core evolution series, with a single failed dynamo at 270 Ma. The frequencies from this series show relatively less variation and fluctuate around $\nu' \approx 8$. Remarkably is the the dynamo at 150 Ma, which generated a strongly dipolar field for which no reversals were detected ($\nu = 0$). The stability of the magnetic field is reflected in the Rm at that time, which is the lowest among all models in any core evolution series and is comparable with those of the candidate models.

6. Discussion

6.1 Setup

Results from both benchmark cases 1 and 2 indicate that the installation of PARODY-JA has been succesful. Namely, all tested quantaties converge either within the margin of uncertainty of the reference value or deviate from those values with an error in the order of 0.1%. Moreover, the spatial distributions of the magnetic and velocity field in case 1 (Fig. 4) are identical to the one presented by Christensen et al. (2001). The fact that $\langle E_{\mathrm{mag}} \rangle$ and ω_{ic} do not converge within the uncertainties might be due to the fact that these uncertainties are not based on statistical analysis, but on a matter of choice (Christensen et al., 2001). That does, however, not imply that the benchmark uncertainties should be overlooked, but should perhaps be regarded as an indication instead of strict criteria.

The strong scaling tests also yields satisfactory results (Fig. 3). That is, the computing time decreases with N_{CPU}, indicating that parallel computations in PARODY-JA are done adequately. For each radial resolution we also find a critical number of CPUs $N_{\mathrm{CPU,crit}}$ after which parallel computations are done less time-efficient. A cause for this criticality is that with increasing N_{CPU} more time is required to communicate between the CPUs and parallelisation becomes less efficient.

6.2 The initial model

The initial model produced a frequency of $\nu = 3.85$ Myr^{-1}, with a relative error to the observed present-day value of 4%. Therefore, it reproduces the reversal behaviour of the present-day geodynamo accurately. Also, this error is agreement with 4.2 Myr^{-1} from the intial model by Olson et al. (2013). Therefore, from the perspective of reversal frequency the initial model is representative of the present-day dynamo so that it could be used to reconstruct geodynamo features.

However, it is debatable whether the initial model can be selected on the basis of reversal frequency alone. An often applied method to

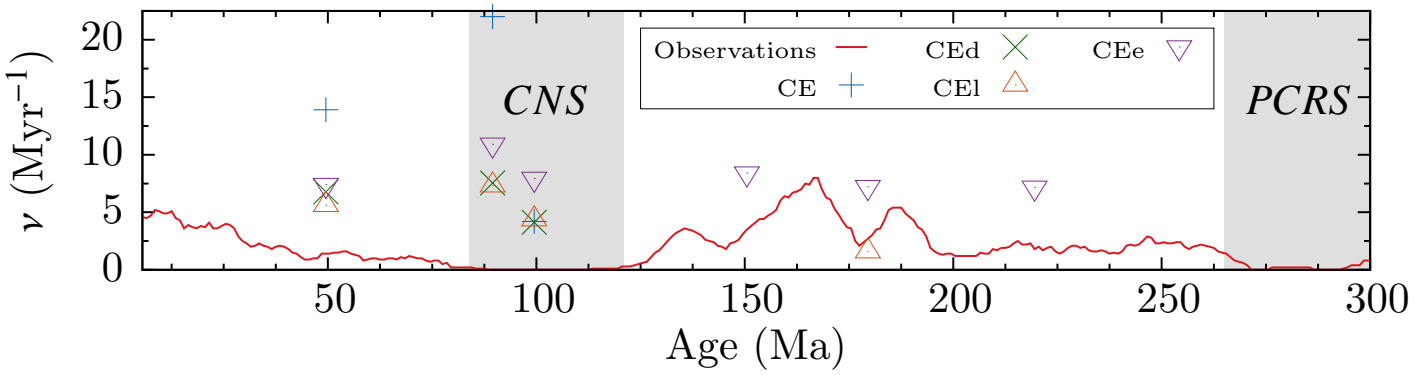

Figure 9: Reversal frequency as a function of time before present. Shown is data from marine- magnetostratigraphic observations (Biggin et al., 2012) and from the reversal frequency scaling law extrapolation of the core evolution series (Table 4). **CE:** core evolution with Q_{cmb} from Biggin et al. (2012). **CEd:** same as CE but with halved secular changes in Q_{cmb}. **CEl:** assumes a linear increase in Q_{cmb}, with the initial and final heat flux as in CE. **CEe:** Same as CEl but with constant E. Gray areas show periods of observed (near) zero reversals frequency (superchrons). A large discrepancy between CE and other series is found. The CEe is the most stable series with relatively small fluctuations and least dynamo failure. A good fit of the CEl and the observations is at 150 Ma.

Age (Ma)	Ra_Q (10^{-4})	E (10^{-4})	χ	δq	F_{icb}/F	τ_r	Ro_l	Rm	ν	ν'
			CE							
50	1.27	2.86	0.339	1.80	0.466	123	0.0448	1632	176	13.9
90	1.09	2.74	0.329	2.15	0.439	117	0.0552	1896	334	22.0
100	1.01	2.70	0.327	1.80	0.434	118	0.0324	1103	-	4.21
150	0.77	2.58	0.314	1.76	0.400	118	×	×	×	×
180	0.73	2.50	0.307	1.59	0.383	200(15)	×	×	×	×
220	0.69	2.40	0.296	1.51	0.356	192(4)	×	×	×	×
270	0.66	2.26	0.282	1.71	0.323	181(4)	×	×	×	×
			CEd							
50	1.22	2.86	0.339	1.80	0.466	122	0.0357	1212	-	6.78
90	1.06	2.74	0.329	2.15	0.439	117	0.0336	1244	390	7.55
100	1.01	2.70	0.327	1.80	0.434	118	0.0323	1135	236	4.13
150	0.83	2.58	0.314	1.76	0.400	175(36)	×	×	×	×
180	0.76	2.50	0.307	1.59	0.383	89(12)	×	×	×	×
220	0.70	2.40	0.296	1.51	0.356	87(10)	×	×	×	×
270	0.63	2.26	0.282	1.71	0.323	8(3)	×	×	×	×
			CEl							
50	1.14	2.86	0.339	1.80	0.466	123	0.0342	1120	270	5.61
90	1.05	2.74	0.329	2.15	0.439	119	0.0333	1180	128	7.30
100	1.02	2.70	0.327	1.80	0.434	116	0.0326	1114	238	4.36
150	0.93	2.58	0.314	1.76	0.400	203(24)	×	×	×	×
180	0.87	2.50	0.307	1.59	0.383	54	0.0307	1079	14.9	1.57
220	0.79	2.40	0.296	1.51	0.356	81(19)	×	×	×	×
270	0.70	2.26	0.282	1.71	0.323	87(3)	×	×	×	×
			CEe							
50	1.32	3.00	0.339	1.80	0.466	65	0.0365	1215	102	7.40
90	1.37	3.00	0.329	2.15	0.439	64	0.0375	1304	349	10.9
100	1.39	3.00	0.327	1.80	0.434	66	0.0372	1217	333	7.94
150	1.46	3.00	0.314	1.76	0.400	64	0.0382	912	0	8.41
180	1.50	3.00	0.307	1.59	0.383	65	0.0384	1365	-	7.22
220	1.55	3.00	0.296	1.51	0.356	65	0.392	1406	239	7.17
270	1.62	3.00	0.282	1.71	0.323	110(8)	×	×	×	×

Table 4: Input and resultant parameters of the core evolution models. For the description of core evolution series notation, see Fig. 9. The reversal frequencies ν are computed by means of the Reversal Detector; the quantities Ro_l, Rm and ν' are obtained by means of the scaling laws given in section 5.1. The brackets in τ_r denote times at which dynamo failure occured. Horizontal lines indicate unavailable data due to an average dipole component $\mu_{|g_1^0|}$ so small that no reversals could be counted ($|g_1^0|$ is always larger than $\mu_{|g_1^0|} - \sigma_{|g_1^0|}$). Crosses indicate failed dynamos: the input parameters did not yield a self-sustainable dynamo solution.

assess whether the produced magnetic field is Earth-like is considering Rm, with the minimum Rm yielding Earth-like fields given by:

$$Rm_{\min} \approx 27 E_\eta^{-2/11} \tag{28}$$

where $E_\eta = E/Pm$ is the magnetic Ekman number. In general the magnetic field is strongly Earth-like when $Rm \sim 2Rm_{\min}$. (Christensen et al., 2010). For our candidate initial models $Rm_{\min} \approx 203$ so that Rm is always well above the minimum (Table 3). However, taking twice the minimum value yields an optimal magnetic Reynolds number of $Rm \sim 400$. All candidate models are characterised by a Rm at least twice as large as that optimal value, of which the initial model has the largest Rm.

Thus, even though appropriate reversal frequencies are produced the candidate models (except in models e. and g.) and $Rm > Rm_{\min}$, Rm might be unrealistically large. The choice for the initial model then becomes particularly debatable, as Rm in the initial model is the largest among all candidate models. While in search of the initial model, one could not only vary Ra_Q as in this study, but also E_η (i.e. a combination of E and Pm). Doing so will alter the optimal Rm and may bring it in closer agreement with that of the candidate models. Then a choice for the initial model can be made based on the obtained reversal frequency and/or Rm. If Rm would have been taken in consideration for the choice of the initial model candidate model d., characterised by a lower frequency but more Earth-like Rm, would have been realistic option.

More uncertainties in the choice for the initial arise from the method of counting reverals. In candidate f. most reversals were counted during $t/\tau_v < 100$, a period in which $|g_1^0|$ was very low (Fig. 6f). Therefore, those reversals might not correspond to the spontaneous change in polarity of the geomagnetic field, but rather to chaotic movement of θ_{dip} due to the negligibility of the dipolar component. In contrast, a more Earth-like reversal is found during the run of candidate b. at $t/\tau_v \approx 60$ (Fig. 6b). At that point, the magnetic field completely switches polarity and a short dip in $|g_1^0|$ is noticeable, of which both event occur within a short period of time i.e. less than $5\tau_v$. Most likely, it is this type of reversal for which the reversal detection algorithm by Lhuillier et al. (2013) was designed, instead of the rather chaotic type. Such chaotic reversals are especially obtained from candidate models e. and g. for which ν and $\mu_{|g_1^0|}$ are abnormally high and low respectively. In both models e. and g. we find long lasting LIES, with some up to 100 t/τ_v. A correlation between the length of LIES and $\mu_{|g_1^0|}$ is thus evident, corresponding to the findings of Lhuillier et al. (2013). One can question whether the algorithm is applied under the right conditions, that is if $|g_1^0|$ was large enough in the candidate models to generate the Earth-like reversals. This issue could be resolved by modifying the algorithm, generating a magnetic field that has a significant dipolar componenent e.g. $|g_1^0| \gtrsim 0.4$ or some combination of the two.

Fluctuations in $\mu_{|g_1^0|}$, θ_{dip} and N_{rev} are stochastic. Determining their behaviour through time is therefore not trivial. Time-averaging these quantities may, however, yield information on how their fluctuations may be described in a general sense. Naturally, an average most representative of a model is found when the average is taken over a sufficient period of time. Unfortunately, it is not clear if the candidate models are in fact run long enough and it is therefore debatable if the corresponding reversal frequencies are representative of the models. For example, candidate a. shows no reversals, although this could be incidental and if the same model is run again it is possible that one or more reversals are found during the run. Thus, because the model has a rather low and high Rm and $\mu_{|g_1^0|}$ respectively, it could be a realistic option for the initial model - despite having no reversals. In any case, a more robust selection of the initial model can be made if the candidate models are run for a longer period, possibly in the order of 500 t/τ_v or larger.

The present-day magnetic field is approximately 90% dipolar, as for example is shown in the 2015 International Geomagnetic Reference Field (Thebault et al., 2015). Therefore, the initial model should have a large dipole component. Candidate b. has the largest $\mu_{|g_1^0|}$ among all reversing candidate models. Thus, when $\mu_{|g_1^0|}$ was also considered a criterion for the selection of the initial model, it would have been a realistic choice. The fact that Rm is relatively low in candidate b. provides additional support for its role as initial model.

6.3 Core evolution

In terms of the reversal frequencies obtained by scaling law extrapolation ν', core evolution models with smaller secular variation in Q_{cmb} reproduce the geodynamo history best. This is best illustrated by the discrepancy between the frequencies of the CE and CEd series (Fig. 9). Being in the same order of magnitude as the observations, the frequencies from the CEd series provide a significantly better fit to the observed reversal record. At 100 Ma the ν' of the CEd, CEl and CEe series show agreement with those obtained with the series by Olson et al. (2013), being just above 4 Myr^{-1}. Unfortunately, all three models were not able to replicate the superchron conditions of the CNS. At 180 Ma the CEl series yields a frequency in close agreement with the observations and the series of Olson et al. (2013), with their model performing slightly better. For times 90 Ma and more recently, the misfit between the series in this work and the their model is large, with the reversals from CEd and CEl a factor 2-3 too large and the reverals in the CE series being unrealistically large.

Secular variations in Q_{cmb} in the CE and CEd series have been as large as 15% and 7.5% respectively, compared to the time average value (Fig. 8). Therefore, considering the better fit of the frequencies in the CEd series, these secular variations have probably not been as higher than 7.5% (Fig. 9). The linear increase in Q_{cmb} as in the CEl series increases the fit slightly with less dynamo failure, enforcing the hypothesis that over the last 270 Myr secular variation in Q_{cmb} has been in the order of 1% and has been characterised by a gradual increase with age. Thus, it is possible that the CMB heat flow reconstruction by Biggin et al. (2012), is not realistic. The reconstruction by Zhang and Zhong (2011) yielded secular variations in Q_{cmb} in the order of $\sim$5% and might therefore be more realistic. That would also explain the success of Olson et al. (2013) who incorporated the reconstruction model of Zhang and Zhong (2011).

The elaboration above is valid under the assumption that the produced fields in the core evolution series is Earth-like. The minimum Rm value for an Earth-like magnetic field ranges from 203 to 214 in the series, so that at all times $Rm > Rm_{\min}$. One may however argue that Rm is too large in the series, at least four times the minimal value. The high Rm values could explain these non-Earth-likeness of the models. For example, the CEl series, in which Rm is low compared to the other series, shows less failure. All magnetic fields from all series are strongly non-dipolar, with the exception of the model at 150 Ma of the CEe series. The multipolar nature of the series also questions the legality of the use of scaling laws to find Ro_l, Rm and ν' as these laws were developed for dipole dominated fields only.

From Fig. 9 one may conclude that, as the discrepancy between the CEd and CEl is negligible, that secular changes in Ra_Q play a minimal role in these reconstructions. Rather, the changes in reversal frequency could be due to changes in other governing parameters, most likely E, χ and δq. Also, due to the fact that dynamo failure is systematically present in each series, it is likely that not the variations in Ra_Q cause the failure, but those in E. For example, a lower E requires Ra_Q to be increasingly supercritical for a dynamo solution to exist (Christensen and Aubert, 2006). In that light, it could be that Q_{cmb} does not increase enough with age to induce that supercriticality, with dynamo failure as a result. This effect could be amplified as in our methods changes in Ra_Q are to proportional those in E to the power three (Eq. (19)), so that a secular decrease in E translates to Ra_Q becoming less supercritical. In the CEe series, secular changes in E have not been incorporated. In contrast to the other series and only the dynamo at 270 Ma fails. Therefore, it indeed appears that E strongly controls whether a numerical dynamo exists or not. More specifically, Ra_Q does not have to

increase with age as much as the other series to ensure the existence of a dynamo solution. However, the dynamo at 270 Ma does fail still, which is likely to be due to the secular decrease of χ and possibly Ra_Q has to compensate for the secular changes in χ as well. This elaboration does, however, not imply that Q_{CMB} does not control reversal frequency. For example, at 100 Ma all evolution series produce an approximately equal ν', which coincides with the fact that in each series $Q_{\mathrm{CMB}} \approx 16$ TW at that time.

The dynamo failure due to E variations could be overcome by choosing a higher E in the initial models so that Ra_Q can be allowed to decrease more with age. For example, in the reversal frequency reconstruction done by Olson et al. (2013), an initial $E(0) = 5.75 \cdot 10^{-3}$ was chosen - more than an order of magnitude higher than in this work. Such a value can be justified by using an appropriate Ra_Q for that $E(0)$. Their $E(0)$ possibly explains why their reconstruction did not yield dynamo failure for ages 150 and beyond. In contrast, Aubert et al. (2009) produced non-failing dynamos for ages over 3 Gyr with an E range similar to this work. However, in their work more supercritical Ra_Q were applied, which might explain their success. In any case, our results demonstrate the importance for a tractable ratio of E to Ra_Q in the initial model, so that Ra_Q can be allowed to change with age.

7. Conclusion

By fitting the reversal record obtained from numerical reconstructions of the geodynamo, an attempt has been made to put constraints on the CMB heat flow and changes therein. To this end the PARODY-JA code was employed and benchmarked succesfully. A number of candidate models have been proposed, with the initial model yielding a reversal frequency of 3.85 Myr^{-1} - in good agreement with the present-day frequency. Several types of CMB heat flow evolution were employed (Fig. 8), as well as estimates for the evolution of other governing parameters. I conclude that:

- the PARODY-JA benchmark using the benchmark study of Christensen et al. (2001) was successful, so that there is a geodynamo code operational at this institute.
- core evolution series with relatively small secular changes in Q_{cmb}, e.g. the CEd and CEl series, recreate the reversal record best. Therefore, it is likely that secular changes in Q_{cmb} have amounted to 7.5% at most, over the past 270 Myr.
- It is likely that Q_{cmb} was characterised by a linear increase with age from roughly 18 to 15 TW over the past 270 Myr.
- secular changes in Q_{cmb} as from Biggin et al. (2012) might be unrealistic, producing too high reversal frequencies or dynamo failure. Another explanation for the failure is that these secular changes are not computationally tractable.
- the value of E in the initial model must not be taken as low as in this work and should be set in the order of 10^{-3} instead. The initial E in this work does not allow Ra_Q to decrease much (roughly 25% at most) before dynamo failure occurs.
- the reversal counting method might not be applicable for dynamos with a small dipole component, e.g. $|\mu_{g_1^0}| < 0.1$. Instead, either the candidate models should be more strongly dipolar and/or the algorithm should be altered to compensate for the effect of chaotic dipole behaviour.

Acknowledgments

Special thanks go out to Julien Aubert for his continuous support and for supplying his code. I thank Andrew Biggin and Bernhard Steinberger for supplying their data and our discussions and my supervisors Lennart de Groot and Cedric Thieulot for their constructive critique and guidance. I am grateful to Paul and Alette whom helped me realise my studies. Lastly, I thank Jasper, Iris and Robert for our time in the 'kamer', and our productive and not so productive interaction.

References

Aubert, J., Labrosse, S., and Poitou, C. (2009). Modelling the palaeo-evolution of the geodynamo. *Geophysical Journal International*, 179:1414–1428.

Biggin, A. J., Steinberger, B., Aubert, J., Suttie, N., Holme, R., Torsvik, T. H., van der Meer, D. G., and van Hinsbergen, D. J. J. (2012). Possible links between long-term geomagnetic variations and whole-mantle convection processes. *Nature Geoscience*, 5:526–533.

Braginsky, S. and Roberts, P. H. (1995). Equations governing convection in Earth's core and the geodynamo. *Geophysical and Astrophysical Fluid Dynamics*, 79:1–97.

Buffett, B. (2012). Earth science: Geomagnetism under scrutiny. *Nature*, 485:355–358.

Buffett, B. A., Huppert, H. E., Lister, J. R., and Woods, A. W. (1996). On the thermal evolution of the earth's core. *Journal of Geophysical Research: Solid Earth*, 101(B4):7989–8006.

Christensen, U. R. and Aubert, J. (2006). Scaling properties of convection-driven dynamos in rotating spherical shells and application to planetary magnetic fields. *Geophysical Journay International*, 166:97–144.

Christensen, U. R., Aubert, J., and Hulot, G. (2010). Conditions for earth-like geodynamo models. *Earth and Planetary Science Letters*, 296:487–496.

Christensen, U. R., J. Aubert, P. C., Dormy, E., Gibbons, S., Glatzmaier, G. A., Grote, E., Honkura, Y., Jones, C., Kono, M., Matsushima, M., Sakuraba, A., Takahashi, F., Tilgner, A., Wicht, J., and Zhang, K. (2001). A numerical dynamo benchmark. *Physics of the Earth and Planetary Interiors*, 128:25–34.

Christensen, U. R. and Tilgner, A. (2004). Power requirement of the geodynamo from ohmic losses in numerical and laboratory dynamos. *Nature*, 429:169–171.

Christensen, U. R. and Wicht, J. (2007). Numerical dynamo simulations. In *Core Dynamics*, volume 8 of *Treatise on Geophysics*, chapter 8, pages 245–279. Elsevier.

Cook, D. M. (2002). *The Theory of the Electromagnetic Field*. Dover Publications, Mineola, New Jersey.

Driscoll, P. and Olson, P. (2009). Polarity reversals in geodynamo models with core evolution. *Earth and Planetary Science Letters*, 282:24–33.

Driscoll, P. and Olson, P. (2011). Superchron cycles driven by variable core heat flow. *Geophysical Research Letters*, 38(9):1–5.

Fleisch, D. (2008). *A Students Guide to Maxwell's Equations*. Cambridge University Press, Cambridge, United Kingdom.

Glatzmaier, G. A., Coe, R. C., Hongre, L., and Roberts, P. H. (1999). The role of the earth's mantle in controlling the frequency of geomagnetic reversals. *Nature*, 401:885–890.

Glatzmaier, G. A. and Coe, R. S. (2007). Magnetic polarity reversals in the core. In *Core Dynamics*, volume 8 of *Treatise on Geophysics*, chapter 9, pages 283–295. Elsevier.

Glatzmaier, G. A. and Roberts, P. H. (1995). A three-dimensional self-consistent computer simulation of a geomagnetic field reversal. *Nature*, 377:203–209.

Kageyama, A. and Sato, T. (1995). Computer simulation of a magnetohydrodynamic dynamo. ii. *Physics of Plasmas*, 2(5):1421–1431.

Labrosse, S., Hernlund, J. W., and Coltice (2007). A crystallizing dense magma ocean at the base of the earth's mantle. *Nature*, 450:866–869.

Larmor, J. (1919). How could a rotating body such as the sun become a magnet? *Reports of the British Association*, 87:159–160.

Lay, T., Hernlund, J., and Buffett, B. A. (2008). Core-mantle boundary heat flow. *Nature Geoscience*, 1:25–32.

Lhuillier, F., Hulot, G., and Gallet, Y. (2013). Statistical properties of reversals and chrons in numerical dynamos and implications for the geodynamo. *Physics of the Earth and Planetary Interiors*, 220:19–36.

Olson, P. (2007). Overview. In *Core Dynamics*, volume 8 of *Treatise on Geophysics*, chapter 1, pages 1–30. Elsevier.

Olson, P. and Christensen, U. R. (2002). The time-averaged magnetic field in numerical dynamos with non-uniform boundary heat flow. *Geophysical Journal International*, 151:809–823.

Olson, P. L. and Amit, H. (2014). Magnetic reversal frequency scaling in dynamos with thermochemical convection. *Physics of the Earth and Planetary Interiors*, 229:122–133.

Olson, P. L., Christensen, U. R., and Driscoll, P. E. (2012). From superchrons to secular variation: A broadband dynamo frequency spectrum for the geomagnetic dipole. *Earth and Planetary Science Letters*, 319-320:75–82.

Olson, P. L., Coe, R. S., Driscoll, P. E., Glatzmaier, G. A., and Roberts, P. H. (2010). Geodynamo reversal frequency and heterogeneous core-mantle boundary heat flow. *Physics of the Earth and Planetary Interiors*, 180(1-2):66–79.

Olson, P. L., Deguen, R., Hinnov, L. A., and Zhong, S. (2013). Controls on geomagnetic reversals and core evolution by mantle convection in the phanerozoic. *Physics of the Earth and Planetary Interiors*, 214:87–103.

Pozzo, M., Davies, C., Gubbins, D., and Alfè, D. (2011). Thermal and electrical conductivity of iron at earth's core conditions. *Nature*, 485:355–358.

Roberts, P. H. (2007). Theory of the geodynamo. In *Core Dynamics*, volume 8 of *Treatise on Geophysics*, chapter 3, pages 67–102. Elsevier.

Steinberger, B. and Torsvik, T. (2010). Toward an explanation for the present and past locations of the poles. *Geochemistry, Geophysics, Geosystems*, 11(6):1–19.

Steinberger, B. and Torsvik, T. (2012). A geodynamic model of plumes from the margins of Large Low Shear Velocity Provinces. *Geochemistry, Geophysics, Geosystems*, 13(1):1–17.

Thebault, E., Finlay, C., Beggan, C., Alken, P., Aubert, J., Barrois, O., Bertrand, F., Bondar, T., Boness, A., Brocco, L., Canet, E., Chambodut, A., Chulliat, A., Coisson, P., Civet, F., Du, A., Fournier, A., Fratter, I., Gillet, N., Hamilton, B., Hamoudi, M., Hulot, G., Jager, T., Korte, M., Kuang, W., Lalanne, X., Langlais, B., Leger, J.-M., Lesur, V., Lowes, F., Macmillan, S., Mandea, M., Manoj, C., Maus, S., Olsen, N., Petrov, V., Ridley, V., Rother, M., Sabaka, T., Saturnino, D., Schachtschneider, R., Sirol, O., Tangborn, A., Thomson, A., Toffner-Clausen, L., Vigneron, P., Wardinski, I., and Zvereva, T. (2015). International geomagnetic reference field: the 12th generation. *Earth, Planets and Space*, 67(1):79.

Williams, G. E. (2000). Geological constraints on the precambrian history of earth's rotation rate and the moon's orbit. *Reviews of Geophysics*, 38:37–59.

Zhang, N. and Zhong, S. (2011). Heat fluxes at the Earth's surface and core-mantle boundary since Pangea formation and their implications for the geomagnetic superchrons. *Earth and Planetary Science Letters*, 306:205–216.

Appendix

A.1 Spherical harmonic conversion

In the following a derivation will be given for the expressions necessary to convert spherical harmonic coefficients from one convention to another. This operation was necessary as the CMB heat flow data was transformed using a different convention than was adopted in PARODY-JA. To be more specific, the coefficients in the data made were in the convention of real valued or tesseral spherical harmonics; those in PARODY-JA were in the regular or complex convention. We start with the conventions used for the data:

$$Y_{lm}(\sigma) = \begin{cases} C_{lm}P_{lm}(\cos\theta)\cos(m\phi) & m \geq 0 \\ C_{lm}P_{l|m|}(\cos\theta)\sin(|m|\phi) & m < 0 \end{cases} \tag{29}$$

$$P_{lm}(x) = (1-x^2)^{\frac{m}{2}}\frac{\mathrm{d}^m}{\mathrm{d}x^m}P_l(x) \tag{30}$$

$$P_l(x) = \frac{1}{2^l l}\frac{\mathrm{d}^l}{\mathrm{d}x^l}\left\{(x^2-1)^l\right\} \tag{31}$$

$$C_{lm} = \sqrt{(2-\delta_{0m})(2l+1)\frac{(l-m)}{(l+m)}} \tag{32}$$

where $Y_{lm}(\sigma) \in \mathbb{R}$ is the tesseral spherical harmonic of degree l and order m, with $l,m \in \mathbb{Z}$ and $m \in [-l,l]$, $P_l(x)$ and $P_{lm}(x)$ the regular and associated Legendre polynomial respectively, C_{lm} a normalisation constant, δ_{ij} is the Kronecker delta, $\sigma = \{\phi,\theta\}$ a coordinate on a spherical surface, $\phi \in [0,2\pi]$ is longitude and $\theta \in [0,\pi]$ is colatitude. On the other hand, we the PARODY-JA conventions, denoted by the prime:

$$Y_l^m(\sigma)' = C_l^{m\prime}P_l^m(\cos\theta)'e^{im\phi} \tag{33}$$

$$P_l^m(x)' = (-1)^m(1-x^2)^{\frac{m}{2}}\frac{\mathrm{d}^m}{\mathrm{d}x^m}P_l(x) \tag{34}$$

$$P_l(x)' = \frac{1}{2^l l}\frac{\mathrm{d}^l}{\mathrm{d}x^l}\left\{(x^2-1)^l\right\} \tag{35}$$

$$C_l^{m\prime} = \sqrt{(2-\delta_{0m})(2l+1)\frac{(l-m)}{(l+m)}} \tag{36}$$

where $Y_l^m(\sigma) \in \mathbb{C}$ is the regular spherical harmonic. We recognize that $C_{lm} = C_l^{m\prime}$ and $P_{lm}(x) = (-1)^m P_l^m(x)'$, allowing us to write the following relation between the harmonics:

$$\begin{aligned} Y_{lm}(\sigma) &= C_l^{m\prime}(-1)^m P_l^{m\prime}(\cos\theta)\cos(m\phi)\,, \quad m \geq 0 \\ &= (-1)^m \mathrm{Re}\left\{Y_l^m(\sigma)'\right\} \\ &= \frac{1}{2}(-1)^m\left(Y_l^m(\sigma)' + \overline{Y}_l^m(\sigma)'\right) \end{aligned} \tag{37}$$

where the overhead line denotes the complex conjugate. One can show that $\overline{Y}_l^m(\sigma) = (-1)^m Y_l^{-m}(\sigma)$, so that the above can be written as

$$Y_{lm}(\sigma) = \frac{1}{2}\left((-1)^m Y_l^m(\sigma)' + Y_l^{-m}(\sigma)'\right)\,, \quad m \geq 0 \tag{38}$$

A similar approach can be followed for negative orders for which we have:

$$Y_{lm} = (-1)^{|m|}C_l^{|m|\prime}P_l^{|m|\prime}(\cos\theta)\sin(|m|\phi)\,, \quad m < 0$$

The moduli in the above expression can be eliminated by recognising that $\forall m < 0 \; |m| = -m$:

$$\begin{aligned} Y_{lm}(\sigma) &= (-1)^{-m} C_l^{-m} P_l^{-m\prime}(\cos\theta)\sin(-m\phi) \\ &= (-1)^{-m}\,\mathrm{Im}\{Y_l^{-m}\} \\ &= \frac{1}{2i}(-1)^{-m}\left(Y_l^{-m\prime} - \overline{Y}_l^{-m\prime}\right) \\ &= \frac{i}{2}\left(Y_l^{m\prime} - (-1)^m Y_l^{-m\prime}\right) \end{aligned} \tag{39}$$

Together, Eq. (38) and (39) show how the tesseral spherical harmonics may be written in terms of the regular type, for nonnegative and negative orders respectively. We now turn to the main objective of this discussion, that is to write the spherical harmonic coefficient $f_l^{m\prime} \in \mathbb{C}$ in terms of $f_{lm} \in \mathbb{R}$. These coefficients allows any function to be decomposed on a spherical surface $F(\sigma) \in \mathbb{C}$ in terms of spherical harmonics:

$$\begin{aligned} F(\sigma) &= \sum_{l=0}^{\infty}\sum_{m=-l}^{l} f_{lm} Y_{lm}(\sigma) \\ &= \sum_{l=0}^{\infty}\sum_{m=-l}^{l} f_l^{m\prime} Y_l^m(\sigma)' \end{aligned} \tag{40}$$

where the coefficient $f_l^{m\prime}$ can by found by evaluating the integral:

$$4\pi f_l^{m\prime} = \int_\Sigma \overline{Y}_l^m(\sigma)' F(\sigma)\,\mathrm{d}\sigma \tag{41}$$

where $\Sigma = [0, 2\pi] \times [0, \pi]$ is the spherical surface. The expression above represents the functional inner product over the spherical surface and can be noted as:

$$4\pi f_l^{m\prime} = \langle \overline{Y}_l^{m\prime}, F \rangle \tag{42}$$

We can substiute Eq. (40) in the above to explicitly write $f_l^{m\prime}$ in terms of f_{lm}:

$$\begin{aligned} 4\pi f_l^{m\prime} &= \left\langle \overline{Y}_l^{m\prime}, \sum_{j=0}^{\infty}\sum_{k=-j}^{j} f_{jk} Y_{jk} \right\rangle \\ &= \sum_{j=0}^{\infty}\sum_{k=-j}^{j} f_{jk}\langle \overline{Y}_l^{m\prime}, Y_{jk}\rangle \\ &= f_{00}(-1)^m \langle \overline{Y}_l^{m\prime}, Y_{00}\rangle + \sum_{j=1}^{\infty}\left\{ \sum_{k=-j}^{-1} f_{jk}\langle \overline{Y}_l^{m\prime}, Y_{jk}\rangle + \sum_{k=0}^{j} f_{jk}\langle \overline{Y}_l^{m\prime}, Y_{jk}\rangle \right\} \end{aligned}$$

The substitution of Eq. (38) and (39) yields the following (dropping the primes):

$$\begin{aligned} 4\pi f_l^m = f_{00}(-1)^m \langle \overline{Y}_l^m, Y_{00}\rangle \quad &+ \quad \frac{1}{2}\sum_{j=1}^{\infty}\left\{ i\sum_{k=-j}^{-1} f_{jk}\left(\langle \overline{Y}_l^m, Y_j^k\rangle - (-1)^k \langle \overline{Y}_l^m, Y_j^{-k}\rangle\right)\right. \\ &+ \quad \left. \sum_{k=0}^{j} f_{jk}\left(\langle \overline{Y}_l^m, Y_j^{-k}\rangle + (-1)^k \langle \overline{Y}_l^m, Y_j^k\rangle\right)\right\} \end{aligned} \tag{43}$$

The regular harmonics are normalised basis functions, such that the their inner product equals:

$$\langle \overline{Y}_l^m, Y_j^k \rangle = 4\pi \delta_{lj}\delta_{mk} \tag{44}$$

This normalisation property allows the inner products in Eq. (43) to eliminated, resulting in the expression:

$$f_l^m = f_{00}(-1)^m \delta_{l0}\delta_{m0} + \frac{1}{2}\sum_{j=1}^{\infty}\delta_{lj}\left\{ i\sum_{k=-j}^{-1} f_{jk}\left(\delta_{mk} - (-1)^k \delta_{m-k}\right) + \sum_{k=0}^{j} f_{jk}\left(\delta_{m-k} + (-1)^k \delta_{mk}\right)\right\}$$

Due to the δ_{lj} factor, the summation is nonzero only when $l > 0$. In that case, the only nonzero term of that summation is the one for which $l = j$. Therefore, we may eliminate the summation sign and only note surviving term:

$$f_l^m = f_{00}(-1)^m \delta_{l0}\delta_{m0} + \frac{1}{2}\left\{ i \sum_{k=-j}^{-1} f_{lk,l>0}\Big(\delta_{mk} - (-1)^k \delta_{m-k}\Big) + \sum_{k=0}^{j} f_{lk,l>0}\Big(\delta_{m-k} + (-1)^k \delta_{mk}\Big) \right\}$$

where $f_{ij,P(i,j)}$ denotes that f_{ij} is zero in the case that the predicate $P(i,j)$ is false. We can apply the same reasoning to the summation over k to find:

$$f_l^m = f_{00}(-1)^m \delta_{l0}\delta_{m0} + \frac{1}{2}\left\{ i\Big(f_{lm,m\in[-l,-1]} - (-1)^m f_{l-m,m\in[1,l]}\Big) + \Big(f_{l-m,m\in[-l,0]} + (-1)^m f_{lm,m\in[0,l]}\Big) \right\}_{l>0}$$

Or as a conditional expression:

$$f_l^m = \begin{cases} \frac{1}{2}(f_{l-m} + i f_{lm}) & m < 0 \\ f_{l0} & m = 0 \\ \frac{1}{2}(-1)^m (f_{lm} - i f_{l-m}) & m > 0 \end{cases} \tag{45}$$

The conditional expression can be understood through the observation that a pair of tesseral coefficients, f_{lm} and f_{l-m}, form a complex pair

$$\phi_{lm} = \begin{cases} f_{lm} & m = 0 \\ f_{l|m|} + i f_{l-|m|} & m \neq 0 \end{cases} \tag{46}$$

such that

$$f_l^m = \begin{cases} \frac{1}{2}\phi_{lm} & m < 0 \\ \phi_{l0} & m = 0 \\ \frac{1}{2}(-1)^m \overline{\phi}_{lm} & m > 0 \end{cases} \tag{47}$$

To conclude, either Eq. (45) or (47) explicitly show how the tesseral spherical harmonic coefficients (f_{lm}) may be converted to the regular kind (f_l^m) for the appropriate orders.

A.2 Reversal Detector source code

Outlined below is the source code of the Reversal Detector used to count the number of reversals during a model run (see section 4.1. The source code and accompanying documentation is available upon request.

`reversal_detector.f90`

```
program reversal_detector
use mod_dipole
implicit none

integer            :: i
integer            :: start_loc,ndat_filt,num_avg
real(8)            :: start_time
logical            :: filter,smooth
character(len=100) :: file_in,file_out

! reading input parameters
read(5,*) file_in
read(5,*) file_out
read(5,*) ndat
read(5,*) filter
read(5,*) start_time
read(5,*) smooth
read(5,*) num_avg

write(6,100) file_in,file_out,ndat,filter,start_time,smooth,num_avg

! allocating arrays
allocate( time(ndat),lat(ndat),fdip(ndat) )

! reading data
call readdipole(ndat,time,lat,fdip,file_in)

! truncating arrays in time
if ( filter ) then
  call start_filter(ndat,ndat_filt,time,lat, start_time)
  call start_filter(ndat,ndat_filt,time,fdip,start_time)
  call start_filter(ndat,ndat_filt,time,time,start_time)
  ndat = ndat_filt
end if

! smoothing dipole strength through moving average
if ( smooth ) then
  call moving_avg(ndat,fdip,num_avg)
  call moving_avg(ndat,lat,num_avg)
end if

! computing dipole strength mean and std. dev.
```

```
call mean_std(ndat,fdip,fdip_mean,fdip_std)

! detecting anomalous events in polarity record
call detector

! writing data to file
call writdat3d(ndat,time,lat,fdip,file_out)
!
!! termination
write(6,200)

! write formats
100 format (                                                  /, &
            '================================================' ,/, &
            'REVERSAL DETECTOR'                               ,/, &
            'Detecting reversals and other events'            ,/, &
            'M.C. Metman, March 2015'                         ,/, &
            '================================================' ,/, &
                                                              /, &
            'reversal_detector.f90: printing parameters'      ,/, &
            'file_in ..................... ',a                ,/, &
            'file_out ..................... ',a               ,/, &
            'ndat ......................... ',i12              ,/, &
            'filter ....................... ',l12              ,/, &
            'start_time ................... ',es12.3           ,/, &
            'smooth ....................... ',l12              ,/, &
            'num_avg ...................... ',i12                 &
           )


200 format (                                                  /, &
            'reversal_detector.f90: FINISHED'                     &
           )

end program
```

readdipole.f90

```
subroutine readdipole(n,x,y,z,filename)
implicit none

integer              :: n,i
real(8)              :: dummy3,dummy4,dummy5,dummy6,dummy7
real(8),dimension(n) :: x,y,z
character(len=*)     :: filename

! opening file
open(11,file=filename)

! reading data
do i=1,n
  read(11,*) x(i),y(i),z(i),dummy4,dummy5,dummy6,dummy7
end do

! conversion from colatitude to latitude
y = 90-y

! taking norm of Gauss coefficient
z = abs(z)

! closing file
close(11)

write(6,300) filename

300 format (                                           /, &
            'readdipole:'                             ,/, &
            'data read from:',1x,A                        &
           )

end subroutine
```

start_filter.f90

```
subroutine start_filter(n,m,x,y,t)
implicit none

integer              :: n,m,i,start_loc
real(8)              :: t
real(8),parameter    :: margin=1d-2
real(8),dimension(n) :: x,y,y2

! copying array
y2 = y

! finding starting location
do i=1,n
  if( abs(x(i)-t) < margin ) then
    start_loc = i
  end if
end do
! new number of data points
m = n-start_loc

! redefining array using new starting location
y(1:m)   = y2(start_loc:m)
! deleting other data points
y(m+1:n) = 0

write(6,400) t,start_loc,m
```

```
400 format (                                    /, &
            'start_filter.f90:'                ,/, &
            'filtered array from t= .......',es12.3,/, &
            'truncated elements ...........',i12   ,/, &
            'new number of data points ....',i12       &
           )

end subroutine
```

moving_avg.f90

```
subroutine moving_avg(ndat,ydat,navg)
implicit none

integer                 :: i,j
integer                 :: ndat,navg,ntrunc
real(8),dimension(ndat) :: ydat
real(8),dimension(ndat) :: yavgdat

! number of nodal points truncated on either domain side
ntrunc = (navg-1)/2

! computing moving average
yavgdat = 0
do i=ntrunc+1,ndat-ntrunc
  do j=i-ntrunc,i+ntrunc
  ! computing average in a single nodal point
    yavgdat(i) = yavgdat(i)+ydat(j)
  end do
  yavgdat(i) = yavgdat(i)/navg
  ! replacing original array with smoothed version
  ydat(i) = yavgdat(i)
end do

end subroutine
```

mean_std.f90

```
subroutine mean_std(n,dat,mean,std)
implicit none

integer              :: n,i
real(8)              :: mean,std
real(8),dimension(n) :: dat

mean = sum(dat)/dble(n)

std = 0.
do i=1,n
  std = std + (dat(i)-mean)**2.
end do
std = sqrt(std/n)

write(6,500) mean,std

open(20,file='mean_std.dat')
!  write(20,'(a,es10.4)') 'STAT1=', mean
!  write(20,'(a,es10.4)') 'STAT2=', mean+std
!  write(20,'(a,es10.4)') 'STAT3=', mean-std
  write(20,*) mean
  write(20,*) mean+std
  write(20,*) mean-std
close(20)

500 format (                                     /, &
            'mean_std.f90:'                     ,/, &
            'computed mean ................. ',es12.3,/, &
            'computed std. dev. ........... ',es12.3    &
           )

end subroutine
```

detector.f90

```
subroutine detector()
use mod_dipole
implicit none

integer :: i,j,k,pos_a,pos_b
integer :: low_count,rev_count,frev_count,sli_count
logical :: pass_equator
real(8) :: low_time(10000)

! initial parameter values
i            = 2
k            = 0
pass_equator = .false.
low_count    = 0
rev_count    = 0
frev_count   = 0
sli_count    = 0

! looping over magnetic record
do while (i <= ndat)
  if( fdip(i) < fdip_mean-fdip_std .and. fdip(i-1) >= fdip_mean-fdip_std ) then
    ! start of low dipole strength period
    low_count = low_count + 1
    ! writing event time
    k = k + 1
    low_time(k) = time(i)
```

```
    pos_a = i
    j = i + 1
    do while ( fdip(j) < fdip_mean-fdip_std .and. j <= ndat )
      if( lat(j)/lat(j-1) < 0 ) then
        ! latitude passed equator
        pass_equator = .true.
      end if
      j = j + 1
    end do
    ! end of low dipole strength period
    pos_b = j - 1
    ! classifying dipole low
    if( lat(pos_b)/lat(pos_a) < 0 ) then
      ! reversal detected
      rev_count = rev_count + 1
    else
      if( pass_equator ) then
        frev_count = frev_count + 1
      else
        sli_count = sli_count + 1
      end if
    end if
    ! setting parameters for next iteration
    pass_equator = .false.
    i = j
    ! writing event time
    k = k + 1
    low_time(k) = time(pos_b)
  else
  ! no dipole low detected
    i = i + 1
  end if
end do

! writing times to file
open(100,file='detector.dat')
write(100,*) low_count
do k=1,2*low_count
  write(100,*) low_time(k)
end do

write(6,500) low_count, rev_count, frev_count,         &
             sli_count,time(ndat)-time(1),             &
             rev_count/(time(ndat)-time(1))

500 format (                                        /, &
            'detector.f90:'                        ,/, &
            'dipole lows counted ..........',i12   ,/, &
            'of which:'                            ,/, &
            '  reversals ..................',i12   ,/, &
            '  failed reversals ...........',i12   ,/, &
            '  SLI events .................',i12   ,/, &
            'over a time period ...........',es12.3,/, &
            'avg. reversal frequency ......',es12.3    &
           )

end subroutine
```

writdat3d.f90

```
subroutine writdat3d(ndat,xdat,ydat,zdat,filename)
implicit none

integer idat,ndat
real(8), dimension(ndat) :: xdat,ydat,zdat
character(len=*) filename

! opening file
open(11,file=filename)

! writing data
do idat=1,ndat
  write(11,*) xdat(idat), ydat(idat), zdat(idat)
end do

write(6,500) filename

500 format (                                          /, &
            'writdat3d:'                             ,/, &
            'output written to:',1x,A                    &
           )

! termination
close(11)

end subroutine
```

A.3 List of symbols and abbreviations

Symbol/Abbreviation	Meaning	Unit	Value	Source
C	Codensity	kg	variable	-
CMB	Core-mantle boundary	-	-	-
CNS	Cretaceous normal superchron	-	-	-
c_P	Heat capacity	J K^{-1}	850	Labrosse et al. (2007)
CPU	Central processing unit or processor	-	-	-
E	(Viscous) Ekman number	-	variable	-
E_λ	Magnetic Ekman number	-	variable	-
emf	Electromotive force	V	-	-
$\langle E_{\mathrm{kin}} \rangle$	Volume averaged kinetic energy	J	variable	-
$\langle E_{\mathrm{mag}} \rangle$	Volume averaged magnetic energy	J	variable	-
$\langle E_{\mathrm{mag,ic}} \rangle$	Volume averaged magnetic energy of the inner core	J	variable	-
$f_i = \alpha_i x^{\beta_i}$	i^{th} power law fit to variable x	-	variable	-
$F = F_{\mathrm{icb}} + F_{\mathrm{cmb}}$	Total mass anomaly flux	kg s^{-1}	variable	-
$F_{\mathrm{icb/cmb}}$	Mass anomaly flux through the ICB/CMB	kg s^{-1}	variable	-
$\lvert g_1^0 \rvert$	Norm of the degree one, order zero Gauss coefficient of the magnetic field	-	variable	-
g_{cmb}	Norm of the gravity field at the CMB	N	variable	-
LIE	Low intensity event	-	-	-
N_{cpu}	Number of CPUs used for model run	-	variable	-
N_{rev}	Number of reversals counted during a model run	-	variable	-
P	Pressure	N m^{-2}	variable	-
PCRS	Permo-Carboniferous reversed superchron	-	-	-
Pm	Magnetic Prandtl number	-	variable	-
Pr	(Thermal) Prandtl number	-	1	e.g. Aubert et al. (2009)
ICB	Inner core boundary	-	-	-
δq	CMB heat flow heterogeneity	-	variable	-
$\overline{q}$	Surface average CMB heat flow	W m^{-2}	variable	-
$q_{\mathrm{min/max}}$	Local minimum/maximum heat flow through the CMB	W m^{-2}	variable	-
Q_{cmb}	Total heat flow through the CMB	W	variable	-
$Q_{\mathrm{cmb,ad}}$	Total adiabatic heat flow through the CMB	W	$6 \cdot 10^{12}$	Aubert et al. (2009)
$r_{\mathrm{icb/cmb}}$	Inner/outer core radius	m	variable	-
Ra	Thermally driven Rayleigh number	-	variable	-
Ra_Q	Bouyancy driven Rayleigh number	-	variable	-
Rm	Magnetic Reynolds number	-	variable	-
Ro_l	Modified Rossby number	-	variable	-
SLIE	Stable low intensity event	-	-	-
T	Temperature	K	variable	-
ΔT Temperature contrast across the outer core	K	1 (benchmark only)	Christensen et al. (2001)	
$\mathbf{B}$	Magnetic field	T	variable	-
$\mathbf{u}$	Flow velocity	m s^{-1}	variable	-
α	Thermal expansion coefficient	K^{-1}	$1.7 \cdot 10^{-5}$	Labrosse et al. (2007)
θ_{dip}	Dipole colatitude	$^\circ$	variable	-
$\mu_{\lvert g_1^0 \rvert}$	Time-average $\lvert g_1^0 \rvert$	-	variable -	
ν	Reversal frequency	yr^{-1}	variable	-
ν'	Reversal frequency obtained from scaling law	yr^{-1}	variable	-
ξ	Mass percentage of light element fraction	-	variable	-
ρ	Mass density	kg m^{-3}	variable	-
$\sigma_{\lvert g_1^0 \rvert}$	Standard deviation of $\lvert g_1^0 \rvert$	-	variable	-
$\Sigma_{\mathrm{icb/cmb}}$	ICB/CMB surface	m^2	variable	-
τ_r	Model run-time	-	variable	-
τ_v	Viscous timescale	yr	$\approx 10^4$	-
τ_λ	Magnetic diffusion timescale	yr	$\approx 2 \cdot 10^5$	Olson et al. (2012)
$\Phi_{\mathrm{icb/cmb}}$	Energetic dissipations through the ICB/CMB	W	variable	-
χ	Inner to outer core radius ratio	-	variable	-
$\psi_{\mathrm{icb/cmb}}$	Gravitational potential at the ICB/CMB	J kg^{-1}	variable	-
$\overline{\psi}$	Outer core average gravitational potential	J kg^{-1}	variable	-
ω_{ic}	Rotation rate of the inner core	s^{-1}	variable	-
Ω	Shell rotation rate	s^{-1}	variable	-